Snake Robots ☆

Kristin Y. Pettersen*

Centre for Autonomous Marine Operations and Systems (NTNU AMOS), Department of Engineering Cybernetics, Norwegian University of Science and Technology, NO-7491 Trondheim, Norway

Abstract

The inspiration for snake robots comes from biological snakes. Snakes display superior mobility capabilities and can move over virtually any type of terrain, including narrow and confined spaces. They are good climbers, very efficient swimmers, and some snakes can even fly by jumping off branches and using their body to glide through the air. Also, a snake robot is a highly articulated robot manipulator arm with the capability of providing its own propulsion.

In this work, we review recent results on modeling, analysis, and control of snake robots moving both on land and underwater. We also describe a new research direction within snake robotics, where underwater snake robots are equipped with thrusters along the body to improve maneuverability and provide hovering capabilities, and how this robot addresses current needs for subsea resident robots in the oil and gas industry.

Keywords: Snake robots, modeling, analysis, control, swimming manipulators

Contents

☆This article is an extended version of a plenary lecture given at the 20th IFAC World Congress, Tolouse, France, 9-14 July, 2017. This work was supported by the Research Council of Norway through the Centres of Excellence funding scheme, project no. 223254 - NTNU AMOS.

*Tel.: +47 73 59 43 46

Email address: Kristin.Y.Pettersen@ntnu.no (Kristin Y. Pettersen)

1. Introduction

The inspiration for snake robots comes from biological snakes. Snakes display excellent mobility capabilities and can move over virtually any type of terrain, including narrow and confined locations. They are good climbers, very efficient swimmers, and some snakes can even fly by jumping off branches and using their body to glide through the air. Also, a snake robot is a highly articulated robot manipulator arm with the capability of providing its own propulsion. These capabilities have spurred an extensive research activity investigating the design and control of snake robots.

A snake robot is a robotic mechanism designed to move like a biological snake. Inspired by the robustness and stability of the locomotion of biological snakes, snake robots carry the potential of meeting the growing need for robotic mobility in unknown and challenging environments. These mechanisms typically consist of many serially connected joint modules capable of bending in one or more planes. The many degrees of freedom of snake robots make them challenging to control, but provide potential locomotion skills in irregular and challenging environments which may surpass the mobility of wheeled, tracked and legged robots (Liljebäck et al. (2012, 2013)).

Research on snake robots has been conducted for several decades. The research field was pioneered about 40 years ago by Professor Shigeo Hirose at Tokyo Institute of Technology, who developed the world's first snake robot as early as 1972 (see Hirose, 1993). The robot, which is shown in Fig. 1, was equipped with passive wheels mounted tangentially along its body. The wheels enabled the robot to travel forward on a flat surface by controlling the joints according to a periodic body wave motion similar to the body waves displayed by biological snakes. In the decades following the pioneering research by Professor Hirose, research communities around the world have developed several agile and impressive snake robots in efforts to mimic the motion capabilities

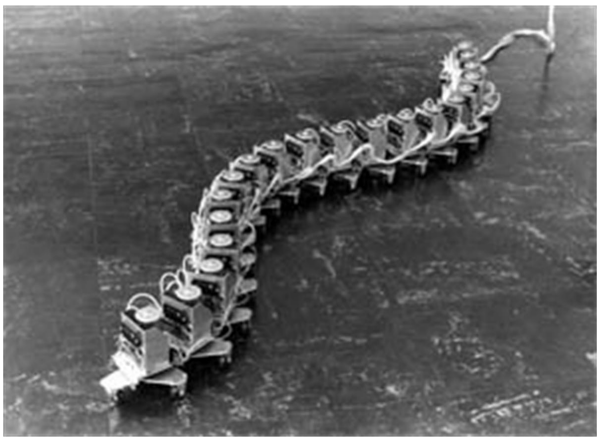

Figure 1: The snake robot *ACM III*, which was the world's first snake robot developed by Prof. Shigeo Hirose in 1972. Courtesy of Tokyo Institute of Technology.

of their biological counterpart. In addition to the research of Shigeo Hirose's group, this includes the seminal works of the research groups of Howie Choset, e.g. (Wright et al. (2007); Tesch et al. (2009)), Auke Ijspeert, (Crespi et al. (2005); Crespi and Ijspeert (2008)), Gregory Chirikjian, (Chirikjian and Burdick (1990, 1995)), Tetsuya Iwasaki, (Prautsch et al. (2000); Saito et al. (2002)), Shugen Ma (Ma (1999, 2001) Jim Ostrowski, (Ostrowski and Burdick (1996); McIsaac and Ostrowski (2003)), and Fumitoshi Matsuno, (Fukushima et al. (2012); Tanaka and Matsuno (2014)). Please note that this list of significant researchers and papers on snake robots is by no means complete, and the reader is referred to the reviews of snake robotics research in Transeth et al. (2008), Hirose and Yamada (2009), Hopkins et al. (2009), Liljebäck et al. (2013), and Sanfilippo et al. (2017) for a more comprehensive exposition.

The present paper reviews a selection of recent work by the author's research group on modeling, analysis, and control of snake robots. A central goal of this work has been to understand the fundamental and inherent properties of snake robots, in order to efficiently control them. The primary focus of our research has thus been on model-based nonlinear analysis and control design. For experimental verification of the theoretical results, we have developed several dedicated snake robots, including Kulko (Fig.2), a snake robot with force sensors, designed for obstacle-aided locomotion; Wheeko (Fig. 3), a snake robot with passive wheels, developed to study snake robot locomotion

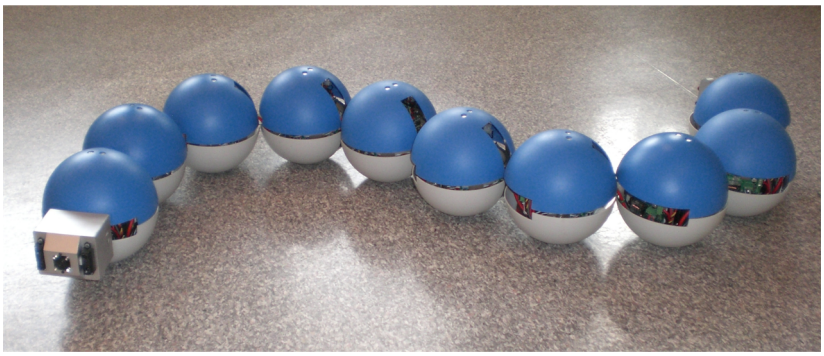

Figure 2: The snake robot *Kulko* developed for locomotion in uneven and cluttered environments.

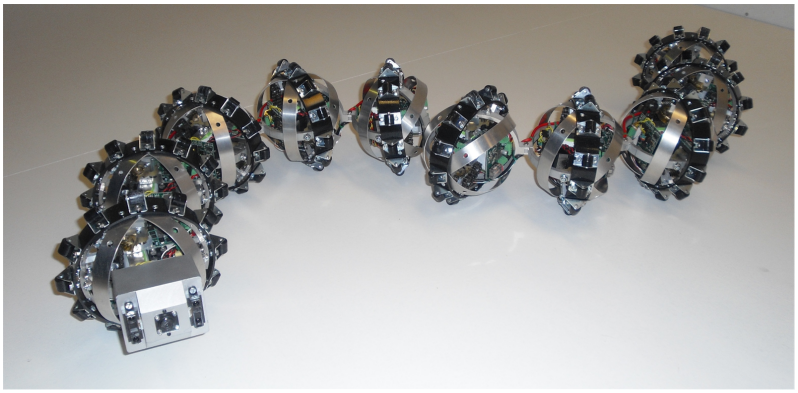

Figure 3: The snake robot *Wheeko* developed for locomotion across flat surfaces.

across flat surfaces; and Mamba (Fig. 4), an amphibious snake robot developed for experimental validation of modeling and control theory of swimming snake robots.

A first goal was thus to derive analytically tractable mathematical models of the snake robots and to utilize these to understand more about the properties of snake robots. The paper starts with a review of mathematical models of snake robots. The kinematics is similar regardless of whether the snake robot moves on land or in water, while the dynamics differs and is presented for snake robots moving on land in Section 2.3 and for snake robots moving underwater in Section 2.4. Then we move on the question of how to make the snake robot move forward. Based on the mathematical models, we see that if the friction or drag force coefficients of a snake robot are larger in the sideways direction than in the longitudinal direction of the robot links, the snake

robot achieves forward propulsion by continuously changing its body shape to induce either ground friction forces or hydrodynamic drag forces that propel the robot forward. When the snake robot follows an undulatory gait pattern, it thus achieves propulsion. Furthermore, the nature of undulatory locomotion allows us to develop simpler mathematical models, which capture the essential behavior of snake robots during undulatory locomotion, and which are well-suited for analysis and control design.

Based on these models, we derive the relationship between the undulatory gait parameters and the forward velocity, such that we can choose the gait parameters to achieve the desired velocity and also make an informed trade-off between speed and power consumption. We then develop path following controllers for the snake robots. For snake robots moving on land, a line-of-sight (LOS) guidance control law is proposed and shown to exponentially stabilize the desired straight line path under a given condition on the look-ahead distance parameter. For snake robots moving underwater, the control law must handle ocean currents of unknown direction and magnitude. To this end, an integral line-of-sight (ILOS) guidance control law is proposed and shown to exponentially stabilize the desired straight line path under given conditions on the look-ahead distance and integral gain parameters. For some applications, it is desirable also to control the forward velocity of the robot. Instead of using tuning of the gait pattern parameters based on the relationship between these parameters and the velocity, which constitute open-loop control of the velocity, we then include feedback control of the forward velocity in the control law, solving the maneuvering control problem. Maneuvering control laws, based on biologically inspired virtual holonomic constraints, are proposed for snake robots moving both on land and underwater.

The paper furthermore presents the underwater swimming manipulator (USM). The USM arises from the question: "What if we combine the best from biology with the best from technology, and equip the snake robot with additional effectors?" This combination of bio-inspiration and technology is also seen in Sarcos' Guardian S, which is a snake-like robot equipped with magnetized tracks (Briggs (2017)), and Boston Dynamics' Handle, which is a humanoid robot with wheels (Guizzo and Ackerman (2017)). The USM combines the slender, multi-articulated and thus flexible body of snakes with the efficient propulsion provided by thrusters. The thrusters give the robot hovering ca-

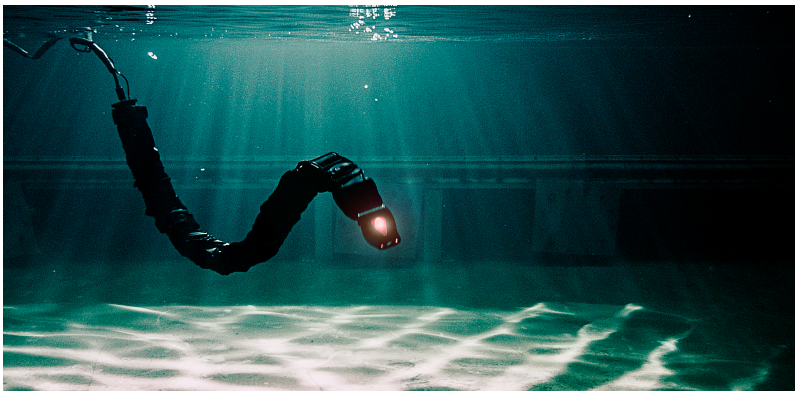

Figure 4: The amphibious snake robot *Mamba*.

pabilities in addition to faster propulsion, while the snake-like body provides the robot with beneficial hydrodynamic properties for long-distance transportation, and exceptional access to narrow areas. In addition, equipping the robot with sensors and tools, the multi-articulated body constitute a dexterous robot manipulator arm that can perform inspection and intervention operations subsea. This robot addresses current needs for subsea resident robots in the oil and gas industry, and also constitute an efficient robotic tool for subsea operations within marine biology, archaeology, aquaculture, and port security.

The paper is organized as follows: Section 2 presents a mathematical model of snake robots moving in 2D on land and underwater. Based on this model, we analyze snake robot locomotion in Section 3. In Section 4 we present a control-oriented model of snake robots, modeling their kinematics and dynamics during undulatory locomotion. In Section 5 we find the relationship between the gait pattern parameters and the resulting forward velocity during undulatory locomotion, based on this model. Section 6 presents solutions to the path following control and maneuvering control problems for snake robots. In Section 7 we introduce the underwater swimming manipulator, and in Section 8 we discuss why the USM is an interesting robotic solution for industrial subsea operations.

2. Mathematical model

This section reviews the mathematical models of snake robots moving on land and in water. In particular, snake robots moving on a horizontal and flat surface on land, and in a 2D plane underwater, are described.

2.1. Notation

We use the following notation throughout this article:

- The operator $\mathrm{diag}(\cdot)$ produces a diagonal matrix with each element of its argument along its diagonal.
- The sign, sine and cosine operators, $\mathrm{sgn}(\cdot)$, $\sin(\cdot)$ and $\cos(\cdot)$, are vector operators when their argument is a vector and scalar operators when their argument is a scalar value.
- We will use subscript i to denote element i of a vector (see Table 1 below). When parameters of the links (joints) of the snake robot are assembled into a vector, we associate element i of this vector with link i (joint i).
- We use a bold font for symbols representing a vector or a matrix.
- The matrix $\mathbf{I_k}$ represents the $k \times k$ identity matrix, and $\mathbf{0}_{i\times j}$ represents the $i \times j$ matrix of zeros.
- A vector related to link i of the snake robot is either expressed in the global coordinate system or in the local coordinate system of the link (see Fig. 5). We indicate the chosen coordinate system by the superscript *global* or $link, i$, respectively. If not otherwise specified, a vector with no superscript is expressed in the global coordinate system.

The snake robot consists of N rigid links of equal length $2l$ interconnected by $N-1$ motorized joints. All N links are assumed to have the same mass m and moment of inertia $J = \frac{1}{3}ml^2$. The mass of each link is uniformly distributed so that the link center of mass (CM) is located at its center point (at length l from the joint on each side).

In the following subsections, we model the kinematics and dynamics of snake robots moving on land and in water using the mathematical symbols described in Table 1 and illustrated in Fig. 5 and Fig. 6. We use the following vectors, matrices and operators in the subsequent sections:

$$\mathbf{A} = \begin{bmatrix} 1 & 1 & & \\ & \ddots & \ddots & \\ & & 1 & 1 \end{bmatrix}, \mathbf{D} = \begin{bmatrix} 1 & -1 & & \\ & \ddots & \ddots & \\ & & 1 & -1 \end{bmatrix}, \tag{1}$$

where $\mathbf{A}, \mathbf{D} \in \mathbb{R}^{(N-1)\times N}$. Furthermore,

$$\mathbf{e} = \begin{bmatrix} 1, \ldots, 1 \end{bmatrix}^T \in \mathbb{R}^N, \mathbf{E} = \begin{bmatrix} \mathbf{e} & \mathbf{0}_{N\times 1} \\ \mathbf{0}_{N\times 1} & \mathbf{e} \end{bmatrix} \in \mathbb{R}^{2N\times 2}, \tag{2}$$

$$\sin\boldsymbol{\theta} = \begin{bmatrix} \sin\theta_1, \ldots, \sin\theta_N \end{bmatrix}^T \in \mathbb{R}^N, \mathbf{S}_\theta = \mathrm{diag}(\sin\boldsymbol{\theta}) \in \mathbb{R}^{N\times N}, \tag{3}$$

$$\cos\boldsymbol{\theta} = \begin{bmatrix} \cos\theta_1, \ldots, \cos\theta_N \end{bmatrix}^T \in \mathbb{R}^N, \mathbf{C}_\theta = \mathrm{diag}(\cos\boldsymbol{\theta}) \in \mathbb{R}^{N\times N} \tag{4}$$

$$\mathrm{sgn}(\boldsymbol{x}) = \begin{bmatrix} \mathrm{sgn}(x_1), \ldots, \mathrm{sgn}(x_n) \end{bmatrix}^T \in \mathbb{R}^n \ \ \forall \boldsymbol{x} \in \mathbb{R}^n \tag{5}$$

$$\boldsymbol{x}^2 = \begin{bmatrix} x_1^2, \ldots, x_n^2 \end{bmatrix}^T \in \mathbb{R}^n \ \ \forall \boldsymbol{x} \in \mathbb{R}^n \tag{6}$$

The matrices $\mathbf{A}$ and $\mathbf{D}$ represent, respectively, an addition and a difference matrix, which we use for adding and subtracting pairs of adjacent elements of a vector. Furthermore, the vector $\mathbf{e}$ represents a summation vector, which will be used for adding all the elements of an N-dimensional vector.

2.2. The kinematics of the snake robot

The kinematics of the snake robot is the same for moving on land and in water, and the material in this section is based on Liljebäck et al. (2013). The snake robot moving on land is assumed to travel on a horizontal and flat surface. The snake robot moving underwater is assumed to travel in a virtual horizontal plane, fully immersed in water. The snake robot has N+2 degrees of freedom (N link angles and the x-y position of the robot). The *link angle* of link $i \in \{1, \ldots, N\}$ of the snake robot is denoted by $\theta_i \in \mathbb{R}$ and

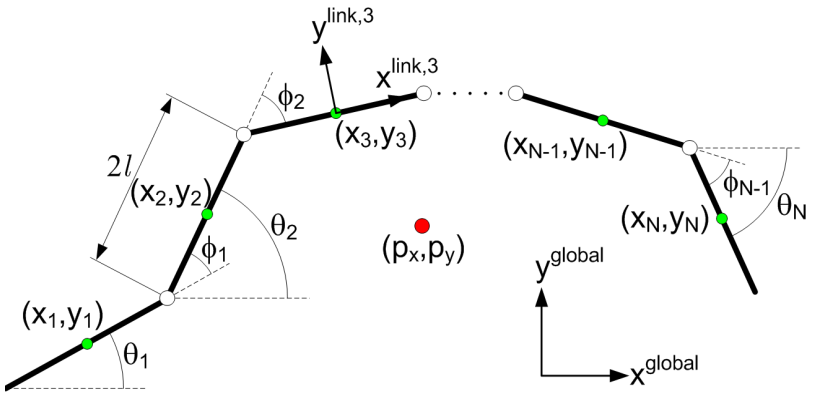

Figure 5: The kinematic parameters of the snake robot.

Table 1: Parameters that characterize the snake robot

Symbol	Description	Vector
N	The number of links	
l	The half length of a link	
m	Mass of each link	
J	Moment of inertia of each link	
θ_i	Angle between link i and the global x-axis	$\boldsymbol{\theta} \in \mathbb{R}^N$
ϕ_i	Angle of joint i	$\boldsymbol{\phi} \in \mathbb{R}^{N-1}$
(x_i, y_i)	Global coordinates of the CM of link i	$\mathbf{X}$,$\mathbf{Y} \in \mathbb{R}^N$
(p_x, p_y)	Global coordinates of the CM of the robot	$\mathbf{p}_{CM} \in \mathbb{R}^2$
u_i	Actuator torque of the joint between link i and link $i+1$	$\mathbf{u} \in \mathbb{R}^{N-1}$
u_{i-1}	Actuator torque of the joint between link i and link $i-1$	$\mathbf{u} \in \mathbb{R}^{N-1}$
$(f_{R,x,i}, f_{R,y,i})$	Ground friction force on link i	$\mathbf{f}_{R,x}$,$\mathbf{f}_{R,y} \in \mathbb{R}^N$
$(f_{x,i}, f_{y,i})$	Fluid force on link i	$\mathbf{f}_\mathbf{x}$,$\mathbf{f}_\mathbf{y} \in \mathbb{R}^N$
τ_i	Fluid torque on link i	$\boldsymbol{\tau} \in \mathbb{R}^N$
$(h_{x,i}, h_{y,i})$	Joint constraint force on link i from link $i+1$	$\mathbf{h}_\mathbf{x}$,$\mathbf{h}_\mathbf{y} \in \mathbb{R}^{N-1}$
$-(h_{x,i-1}, h_{y,i-1})$	Joint constraint force on link i from link $i-1$	$\mathbf{h}_\mathbf{x}$,$\mathbf{h}_\mathbf{y} \in \mathbb{R}^{N-1}$

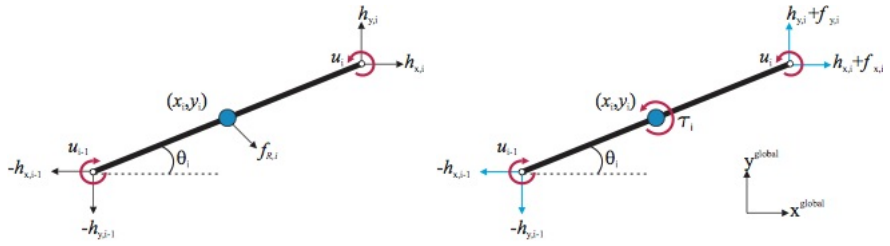

(a) Moving on land (b) Moving in water

Figure 6: Forces and torques acting on each link

is defined as the angle that the link forms with the global x-axis, while the *joint angle* of joint $i \in \{1,\ldots,N-1\}$ is denoted $\phi_i \in \mathbb{R}$ and defined as

$$\phi_i = \theta_i - \theta_{i+1} \qquad i = 1,\ldots,N-1. \tag{7}$$

In other words, the *link angle* is the orientation of a link with respect to the global x-axis, while the joint angle is the angle between two adjacent links. The link angles and the joint angles are assembled in the vectors $\boldsymbol{\theta} = [\theta_1,\ldots,\theta_N]^T \in \mathbb{R}^N$ and $\boldsymbol{\phi} = [\phi_1,\ldots,\phi_{N-1}]^T \in \mathbb{R}^{N-1}$, respectively. There are several alternatives for defining the orientation of the snake robot. A common choice is defining the *orientation* (or *heading*) $\bar{\theta} \in \mathbb{R}$ of the snake as the average of the link angles (Hatton and Choset (2009); Hu et al. (2009); Liljebäck et al. (2013)):

$$\bar{\theta} = \frac{1}{N}\sum_{i=1}^{N}\theta_i. \tag{8}$$

175

Remark 1. *Note that there is no unique definition for the orientation of a snake robot. Equation 8 gives one of several alternative measures. Other measures may for instance be the heading of the head link or the orientation of the velocity vector of the CM. Which definition to choose will depend on what our control objectives are.*

The kinematics of the snake robot is derived using link angles instead of joint angles, as this simplifies the mathematical expressions. We position the local coordinate system of each link in the CM of the link with the x- (tangential) and y- (normal) axis oriented

such that they align with the global x- and y-axis, respectively, when all the link angles are zero. The rotation matrix from the global frame to the frame of link i is

$$\mathbf{R}_{\text{link},i}^{\text{global}} = \begin{bmatrix} \cos\theta_i & -\sin\theta_i \\ \sin\theta_i & \cos\theta_i \end{bmatrix}. \tag{9}$$

The global frame position $\mathbf{p}_{\text{CM}} \in \mathbb{R}^2$ of the CM of the robot is given by

$$\mathbf{p}_{\text{CM}} = \begin{bmatrix} p_x \\ p_y \end{bmatrix} = \begin{bmatrix} \frac{1}{Nm}\sum_{i=1}^{N} m x_i \\ \frac{1}{Nm}\sum_{i=1}^{N} m y_i \end{bmatrix} = \frac{1}{N}\begin{bmatrix} \mathbf{e}^T\mathbf{X} \\ \mathbf{e}^T\mathbf{Y} \end{bmatrix}, \tag{10}$$

where (x_i, y_i) are the global frame coordinates of the CM of link i, $\mathbf{X} = [x_1, \ldots, x_N]^T \in \mathbb{R}^N$ and $\mathbf{Y} = [y_1, \ldots, y_N]^T \in \mathbb{R}^N$. The *forward velocity* of the robot is denoted by $\bar{v}_t \in \mathbb{R}$ and is defined as the component of the CM velocity $\dot{\mathbf{p}}_{\text{CM}}$ along the current orientation of the snake robot, $\bar{\theta}$, i.e. as

$$\bar{v}_t = \dot{p}_x \cos\bar{\theta} + \dot{p}_y \sin\bar{\theta}. \tag{11}$$

where the subscript t denotes *tangential.*

The connection between the adjacent links i and $i+1$ at joint $i \in \{1, \ldots, N-1\}$ has to comply with the two holonomic constraints

$$x_{i+1} - x_i = l\cos\theta_i + l\cos\theta_{i+1}, \tag{12a}$$

$$y_{i+1} - y_i = l\sin\theta_i + l\sin\theta_{i+1}. \tag{12b}$$

Using the notation from Section 2.1, we can write the joint constraints for all the links of the robot in matrix form as

$$\mathbf{D}\mathbf{X} + l\mathbf{A}\cos\boldsymbol{\theta} = \mathbf{0}, \tag{13a}$$

$$\mathbf{D}\mathbf{Y} + l\mathbf{A}\sin\boldsymbol{\theta} = \mathbf{0}. \tag{13b}$$

We can now express the position of the individual links as a function of the CM position and the link angles of the robot by combining (10) and (13) into

$$\mathbf{TX} = \begin{bmatrix} -l\mathbf{A}\cos\boldsymbol{\theta} \\ \\ p_x \end{bmatrix}, \quad \mathbf{TY} = \begin{bmatrix} -l\mathbf{A}\sin\boldsymbol{\theta} \\ \\ p_y \end{bmatrix}, \tag{14}$$

where

$$\mathbf{T} = \begin{bmatrix} \mathbf{D} \\ \\ \frac{1}{N}\mathbf{e}^T \end{bmatrix} \in \mathbb{R}^{N\times N}. \tag{15}$$

It can be shown that

$$\mathbf{T}^{-1} = \begin{bmatrix} \mathbf{D}^T\left(\mathbf{D}\mathbf{D}^T\right)^{-1} & \mathbf{e} \end{bmatrix}, \tag{16}$$

which enables us to solve (14) for $\mathbf{X}$ and $\mathbf{Y}$ according to

$$\mathbf{X} = \mathbf{T}^{-1}\begin{bmatrix} -l\mathbf{A}\cos\boldsymbol{\theta} \\ \\ p_x \end{bmatrix} = -l\mathbf{K}^T\cos\boldsymbol{\theta} + \mathbf{e}p_x, \tag{17a}$$

$$\mathbf{Y} = \mathbf{T}^{-1}\begin{bmatrix} -l\mathbf{A}\sin\boldsymbol{\theta} \\ \\ p_y \end{bmatrix} = -l\mathbf{K}^T\sin\boldsymbol{\theta} + \mathbf{e}p_y, \tag{17b}$$

where $\mathbf{K} = \mathbf{A}^T\left(\mathbf{D}\mathbf{D}^T\right)^{-1}\mathbf{D} \in \mathbb{R}^{N\times N}$, and where $\mathbf{D}\mathbf{D}^T$ is nonsingular and thereby invertible Liljebäck et al. (2013).

We find the linear velocities of the links by differentiating the position of the individual links (17a) and (17b) with respect to time, which gives

$$\dot{\mathbf{X}} = l\mathbf{K}^T\mathbf{S}_\theta\dot{\boldsymbol{\theta}} + \mathbf{e}\dot{p}_x, \quad \dot{\mathbf{Y}} = -l\mathbf{K}^T\mathbf{C}_\theta\dot{\boldsymbol{\theta}} + \mathbf{e}\dot{p}_y. \tag{18}$$

By manually investigating the structure of each row in (18), it can be verified that the linear velocity of the CM of link i in the global x and y directions is given by

$$\dot{x}_i = \dot{p}_x - \boldsymbol{\sigma}_i\mathbf{S}_\theta\dot{\boldsymbol{\theta}}, \tag{19a}$$

$$\dot{y}_i = \dot{p}_y + \boldsymbol{\sigma}_i\mathbf{C}_\theta\dot{\boldsymbol{\theta}}, \tag{19b}$$

where

$$\boldsymbol{\sigma}_i = \left[a_1, a_2, \ldots, a_{i-1}, \frac{a_i + b_i}{2}, b_{i+1}, b_{i+2}, \ldots, b_N\right] \tag{20a}$$

$$a_i = \frac{l\,(2i-1)}{N}, b_i = \frac{l\,(2i-1-2N)}{N}. \tag{20b}$$

The notation and model derivations presented above are based on (Liljebäck et al., 2013, Chapter 2) where further details can be found for snake robots moving on land. For modeling the dynamics of the underwater snake robot in Section 2.4, it is necessary also to derive the equations of the linear acceleration of the links in order to express the fluid forces. We find the linear accelerations of the links by differentiating the velocity of the individual links (18) with respect to time, which gives (Kelasidi et al. (2014c)):

$$\begin{aligned} \ddot{\mathbf{X}} &= l\mathbf{K}^T\left(\mathbf{C}_\theta \dot{\boldsymbol{\theta}}^2 + \mathbf{S}_\theta \ddot{\boldsymbol{\theta}}\right) + \mathbf{e}\ddot{p}_x, \\ \ddot{\mathbf{Y}} &= l\mathbf{K}^T\left(\mathbf{S}_\theta \dot{\boldsymbol{\theta}}^2 - \mathbf{C}_\theta \ddot{\boldsymbol{\theta}}\right) + \mathbf{e}\ddot{p}_y. \end{aligned} \tag{21}$$

2.3. The dynamics of snake robots moving on land

In this section we present the dynamics of a snake robot moving on a horizontal and flat surface. As we will see in Section 3, the ground friction properties are decisive for snake robot motion. We will start by presenting the ground friction model, and then present the mathematical equations describing the dynamics of snake robots moving on land. The material in this section is based on Liljebäck et al. (2013).

2.3.1. Ground friction model

We assume that the ground friction force on a link is proportional to the velocity of the link, i.e. we use a viscous friction model, and we assume that the viscous ground friction forces act on the CM of the links.

Isotropic viscous friction

The isotropic viscous friction force on link i in the global x and y direction is proportional to the global frame velocity of the link given by (19) and is given by

$$\mathbf{f}_{R,i} = \mathbf{f}_{R,i}^{\text{global}} = -c \begin{bmatrix} \dot{x}_i \\ \dot{y}_i \end{bmatrix} = -c \begin{bmatrix} \dot{p}_x - \boldsymbol{\sigma}_i \mathbf{S}_\theta \dot{\boldsymbol{\theta}} \\ \dot{p}_y + \boldsymbol{\sigma}_i \mathbf{C}_\theta \dot{\boldsymbol{\theta}} \end{bmatrix}, \tag{22}$$

where c is the viscous friction coefficient. The friction forces on all links can be written in matrix form as

$$\mathbf{f}_R = \begin{bmatrix} \mathbf{f}_{R,x} \\ \mathbf{f}_{R,y} \end{bmatrix} = -c \begin{bmatrix} \dot{\mathbf{X}} \\ \dot{\mathbf{Y}} \end{bmatrix} = -c \begin{bmatrix} l\mathbf{K}^T \mathbf{S}_\theta \dot{\boldsymbol{\theta}} + \mathbf{e}\dot{p}_x \\ -l\mathbf{K}^T \mathbf{C}_\theta \dot{\boldsymbol{\theta}} + \mathbf{e}\dot{p}_y \end{bmatrix}, \tag{23}$$

where we have used the expression for the link velocities given by (18), and where $\mathbf{f}_{R,x} = [f_{R,x,1}, \ldots, f_{R,x,N}]^T \in \mathbb{R}^N$ and $\mathbf{f}_{R,y} = [f_{R,y,1}, \ldots, f_{R,y,N}]^T \in \mathbb{R}^N$ contain the friction forces on the links in the global x and y direction, respectively.

Anisotropic viscous friction

Under anisotropic friction conditions, a link has two viscous friction coefficients, c_t and c_n, describing the friction force in the tangential (along the link x axis) and normal (along the link y axis) direction of the link, respectively. We define the viscous friction force on link i in the local link frame, $\mathbf{f}_{R,i}^{\text{link},i} \in \mathbb{R}^2$, as

$$\mathbf{f}_{R,i}^{\text{link},i} = - \begin{bmatrix} c_t & 0 \\ 0 & c_n \end{bmatrix} \mathbf{v}_i^{\text{link},i}, \tag{24}$$

where $\mathbf{v}_i^{\text{link},i} \in \mathbb{R}^2$ is the link velocity expressed in the local link frame. By using (9), we can express the global frame viscous friction force on link i as

$$\begin{aligned} \mathbf{f}_{R,i} = \mathbf{f}_{R,i}^{\text{global}} &= \mathbf{R}_{\text{link},i}^{\text{global}} \mathbf{f}_{R,i}^{\text{link},i} = -\mathbf{R}_{\text{link},i}^{\text{global}} \begin{bmatrix} c_t & 0 \\ 0 & c_n \end{bmatrix} \mathbf{v}_i^{\text{link},i} \\ &= -\mathbf{R}_{\text{link},i}^{\text{global}} \begin{bmatrix} c_t & 0 \\ 0 & c_n \end{bmatrix} \left(\mathbf{R}_{\text{link},i}^{\text{global}} \right)^T \begin{bmatrix} \dot{x}_i \\ \dot{y}_i \end{bmatrix}, \end{aligned} \tag{25}$$

By performing the matrix multiplication in (25), we get

$$\mathbf{f}_{R,i} = -\begin{bmatrix} c_t\cos^2\theta_i + c_n\sin^2\theta_i & (c_t-c_n)\sin\theta_i\cos\theta_i \\ (c_t-c_n)\sin\theta_i\cos\theta_i & c_t\sin^2\theta_i + c_n\cos^2\theta_i \end{bmatrix}\begin{bmatrix}\dot{x}_i \\ \dot{y}_i\end{bmatrix}. \tag{26}$$

By assembling the forces on all links in matrix form, the global frame viscous friction forces on the links can be written as

$$\mathbf{f}_R = \begin{bmatrix}\mathbf{f}_{R,x} \\ \mathbf{f}_{R,y}\end{bmatrix} = -\begin{bmatrix} c_t\left(\mathbf{C}_\theta\right)^2 + c_n\left(\mathbf{S}_\theta\right)^2 & (c_t-c_n)\mathbf{S}_\theta\mathbf{C}_\theta \\ (c_t-c_n)\mathbf{S}_\theta\mathbf{C}_\theta & c_t\left(\mathbf{S}_\theta\right)^2 + c_n\left(\mathbf{C}_\theta\right)^2 \end{bmatrix}\begin{bmatrix}\dot{\mathbf{X}} \\ \dot{\mathbf{Y}}\end{bmatrix} \in \mathbb{R}^{2N}. \tag{27}$$

Note that (27) reduces to (23) in the case of isotropic friction, i.e. when $c_t = c_n = c$.

2.3.2. The dynamics of the snake robot

The $N+2$ degrees of freedom of the snake robot are defined by the link angles $\boldsymbol{\theta} \in \mathbb{R}^N$ and the CM position $\mathbf{p}_{\text{CM}} \in \mathbb{R}^2$. We now present the equations of motion of the robot expressed by the acceleration of the link angles, $\ddot{\boldsymbol{\theta}}$, and the acceleration of the CM position, $\ddot{\mathbf{p}}_{\text{CM}}$. The details of the derivation of these equations can be found in Liljebäck et al. (2013).

$$\mathbf{M}_\theta\ddot{\boldsymbol{\theta}} + \boldsymbol{W}\dot{\boldsymbol{\theta}}^2 - l\mathbf{S}_\theta\mathbf{K}\mathbf{f}_{R,x} + l\mathbf{C}_\theta\mathbf{K}\mathbf{f}_{R,y} = \mathbf{D}^T\mathbf{u}, \tag{28a}$$

$$Nm\ddot{\mathbf{p}}_{\text{CM}} = Nm\begin{bmatrix}\ddot{p}_x \\ \ddot{p}_y\end{bmatrix} = \begin{bmatrix}\mathbf{e}^T\mathbf{f}_{R,x} \\ \mathbf{e}^T\mathbf{f}_{R,y}\end{bmatrix} = \mathbf{E}^T\mathbf{f}_R, \tag{28b}$$

where $\mathbf{f}_R$ is the viscous friction force given by (27), and where

$$\mathbf{M}_\theta = J\mathbf{I}_N + ml^2\mathbf{S}_\theta\mathbf{V}\mathbf{S}_\theta + ml^2\mathbf{C}_\theta\mathbf{V}\mathbf{C}_\theta, \tag{29a}$$

$$\mathbf{W} = ml^2\mathbf{S}_\theta\mathbf{V}\mathbf{C}_\theta - ml^2\mathbf{C}_\theta\mathbf{V}\mathbf{S}_\theta, \tag{29b}$$

$$\mathbf{V} = \mathbf{A}^T\left(\mathbf{D}\mathbf{D}^T\right)^{-1}\mathbf{A}, \tag{29c}$$

$$\mathbf{K} = \mathbf{A}^T\left(\mathbf{D}\mathbf{D}^T\right)^{-1}\mathbf{D}. \tag{29d}$$

By introducing the state variable $\mathbf{x} = \begin{bmatrix} \boldsymbol{\theta}^T & \mathbf{p}_{\text{CM}}^T & \dot{\boldsymbol{\theta}}^T & \dot{\mathbf{p}}_{\text{CM}}^T \end{bmatrix}^T \in \mathbb{R}^{2N+4}$, the model of the snake robot can be written compactly in state space form as

$$\dot{\mathbf{x}} = \begin{bmatrix} \dot{\boldsymbol{\theta}} \\ \dot{\mathbf{p}}_{\text{CM}} \\ \ddot{\boldsymbol{\theta}} \\ \ddot{\mathbf{p}}_{\text{CM}} \end{bmatrix} = \mathbf{F}(\mathbf{x}, \mathbf{u}), \tag{30}$$

where the elements of $\mathbf{F}(\mathbf{x}, \mathbf{u})$ are easily found by solving (28a) and (28b) for $\ddot{\boldsymbol{\theta}}$ and $\ddot{\mathbf{p}}_{\text{CM}}$, respectively.

To express the dynamics in a control affine form, a partial feedback linearisation which includes a separation of the actuated and the unactuated part of the dynamics, is presented in (Liljebäck et al., 2013, Chapter 2.8). In particular, the new state vector is defined by $\mathbf{x}_1 = \mathbf{q}_a$, $\mathbf{x}_2 = \mathbf{q}_u$, $\mathbf{x}_3 = \dot{\mathbf{q}}_a$, $\mathbf{x}_4 = \dot{\mathbf{q}}_u$, and $\mathbf{x} = \begin{bmatrix} \mathbf{x}_1^T, \mathbf{x}_2^T, \mathbf{x}_3^T, \mathbf{x}_4^T \end{bmatrix}^T \in \mathbb{R}^{2N+4}$, where $\mathbf{q}_a = [\phi_1, \ldots, \phi_{N-1}]^T \in \mathbb{R}^{N-1}$ represents the actuated degrees of freedom, $\mathbf{q}_u = [\theta_N, p_x, p_y]^T \in \mathbb{R}^3$ represents the unactuated degrees of freedom. The partial feedback linearization gives a new set of control inputs, $\overline{\mathbf{u}} = [\overline{u}_1, \ldots, \overline{u}_{N-1}]^T \in \mathbb{R}^{N-1}$, and the resulting system is then given in the control-affine form

$$\dot{\mathbf{x}} = \begin{bmatrix} \dot{\mathbf{x}}_1 \\ \dot{\mathbf{x}}_2 \\ \dot{\mathbf{x}}_3 \\ \dot{\mathbf{x}}_4 \end{bmatrix} = \mathbf{f}(\mathbf{x}) + \sum_{j=1}^{N-1} \left(\mathbf{g}_j(\mathbf{x}_1) \overline{u}_j \right). \tag{31}$$

The mathematical model can also be extended to include contact forces from interaction with obstacles in the environment around the robot. Since the interaction with an obstacle represents a discrete event that only occurs when a link of the robot comes into contact with the obstacle, the snake robot model will then incorporate both continuous and discontinuous dynamics. The resulting hybrid model can be found in Liljebäck et al. (2013).

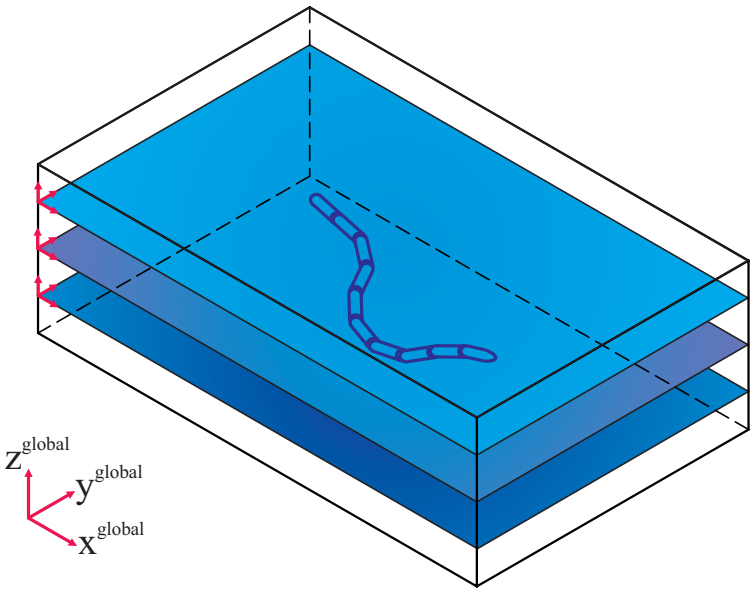

Figure 7: Visualization of a ten link snake robot moving fully submerged in a virtual horizontal plane.

2.4. The dynamics of snake robots moving underwater

In this section we present the dynamics of a snake robot moving in a virtual horizontal plane, i.e. moving at a constant depth, fully immersed in water as shown in Fig. 7. The snake robot is assumed to be neutrally buoyant, such that its depth remains constant unless active depth control is used (using the rotation of the links around the body-fixed y-axis). The material in this section is based on Kelasidi et al. (2014b,c, 2017b).

2.4.1. Hydrodynamic forces and torques

The underwater snake robots will swim at Reynolds numbers between 10^4 and 10^5, and this entails that both resistive forces (drag forces) and reactive forces (added mass effects) need to be modeled since both will have a decisive effect on the propulsion of the swimming snake robot (Wiens and Nahon (2012)). The model is derived under the following assumptions:

Assumption 1. *The fluid is viscid, incompressible, and irrotational in the inertial frame.*

Assumption 2. *The robot is neutrally buoyant.*

Assumption 3. *The ocean current velocity in the inertial frame, $v_c = [V_x, V_y]^T$, is constant and irrotational.*

Remark 2. *Assumptions 1 and 2 are common assumptions in hydrodynamic modeling of slender body swimming robots (Boyer et al. (2006a); Wiens and Nahon (2012)), while Assumption 3 is a reasonable simplification of the real-world situation and is a standard assumption in marine control theory (Fan and Woolsey (2013); Fossen (2011)).*

Remark 3. *Neutral buoyancy, i.e. that the mass per unit of volume of the robot is equal to that of the water, such that gravity and buoyancy cancel each other, is achieved by proper ballasting of the snake robot. The ballast will furthermore be positioned at the bottom of each snake robot link, to prevent it from rolling, making it self-stabilized in roll.*

Assumption 4. *The relative velocity at each section of the link in the body-fixed frame is equal to the relative velocity of the respective center of mass of each link.*

Remark 4. *This approximation is valid when the link length is small compared to the length of the total robot, which means that the linear velocity of each point along a link will be approximately the same. Due to Assumption 4 it is not necessary to numerically evaluate the drag forces using an algorithmic approach of modeling, and we derive instead a compact and closed-form model that is suited for model-based analysis and control.*

The hydrodynamic forces (fluid forces) are expressed as functions of the relative velocity, where the relative velocity of link i is defined as $v_{r,i}^{\text{link},i} = \dot{p}_i^{\text{link},i} - v_{c,i}^{\text{link},i}$, where $v_{c,i}^{\text{link},i} = (\mathbf{R}_{\text{link},i}^{\text{global}})^T v_c = [v_{x,i}, v_{y,i}]^T$ is the ocean current velocity expressed in the body-fixed frame coordinates, and $v_c = [V_x, V_y]^T$ is the ocean current velocity expressed in inertial frame coordinates. Due to Assumption 3, $\dot{v}_c = 0$ and thus

$$\dot{v}_{c,i}^{\text{link},i} = \frac{d}{dt}\left((\mathbf{R}_{\text{link},i}^{\text{global}})^T v_c\right) = \begin{bmatrix} -\sin\theta_i\dot{\theta}_i & \cos\theta_i\dot{\theta}_i \\ -\cos\theta_i\dot{\theta}_i & -\sin\theta_i\dot{\theta}_i \end{bmatrix} \begin{bmatrix} V_x \\ V_y \end{bmatrix}. \tag{32}$$

Each link of the robot is subject to a force from the fluid acting on the CM of the link and also a fluid torque acting on the CM. In the following, we will present the fluid forces and torques acting on the snake robot. In particular, we present how the force exerted by the fluid on a cylindrical object is made up of two components: the virtual mass force (added mass effect) and the drag force. The drag model takes into account the generalized case of anisotropic resistive (drag) forces acting on each link. The anisotropy means that each link has two drag coefficients, c_t and c_n, describing the drag force in the tangential (along the link x axis) and normal (along the link y axis) direction of the link, respectively.

The **fluid forces** exerted on link i by the fluid are

$$f_i^{\text{link},i} = -\hat{\mathbf{C}}_A \dot{v}_{r,i}^{\text{link},i} - \hat{\mathbf{C}}_D v_{r,i}^{\text{link},i} - \hat{\mathbf{C}}_D \,\text{diag}(\text{sgn}\left(v_{r,i}^{\text{link},i}\right)) \left(v_{r,i}^{\text{link},i}\right)^2, \tag{33}$$

where $\dot{v}_{r,i}^{\text{link},i} = \ddot{p}_i^{\text{link},i} - \dot{v}_{c,i}^{\text{link},i}$ is the relative acceleration of link i, $\dot{p}_i^{\text{link},i}$ and $\ddot{p}_i^{\text{link},i}$ are the velocity and the acceleration of link i, respectively, expressed in the body frame. The matrices $\hat{\mathbf{C}}_A$ and $\hat{\mathbf{C}}_D$ are constant diagonal (2×2) matrices depending on the shape of the body and the fluid characteristics. For cylindrical links with major diameter $2a$ and minor diameter $2b$, and taking into account that the length of each link is $2l$, the matrices $\hat{\mathbf{C}}_A$, $\hat{\mathbf{C}}_D$ are

$$\hat{\mathbf{C}}_A = \begin{bmatrix} \mu_t & 0 \\ 0 & \mu_n \end{bmatrix} = \begin{bmatrix} 0 & 0 \\ 0 & \rho\pi C_A a^2 2l \end{bmatrix}, \tag{34}$$

$$\hat{\mathbf{C}}_D = \begin{bmatrix} c_t & 0 \\ 0 & c_n \end{bmatrix} = \begin{bmatrix} \frac{1}{2}\rho\pi C_f \frac{(b+a)}{2} 2l & 0 \\ 0 & \frac{1}{2}\rho C_D 2a 2l \end{bmatrix}, \tag{35}$$

where C_f and C_D are the drag coefficients in the body-fixed x- (tangential) and y- (normal) direction of the links, ρ is the density of the fluid, and C_A denotes the added mass coefficient in the normal direction. Since we assume that the USR is fully immersed in water, below the wave zone, the added mass parameters μ_t and μ_n are constant (i.e. equal to the asymptotic values when the wave frequency is going to zero).

The added mass parameter in the x-direction is considered equal to zero ($\mu_t = 0$) because the added mass of a slender body in the longitudinal direction can be neglected compared to the body mass Newman (1977).

By assembling the fluid forces acting on all links in a vector, the fluid forces on the links expressed in the global frame can be written as

$$\mathbf{f} = \begin{bmatrix} \mathbf{f_x} \\ \mathbf{f_y} \end{bmatrix} = \begin{bmatrix} \mathbf{f_{A_x}} \\ \mathbf{f_{A_y}} \end{bmatrix} + \begin{bmatrix} \mathbf{f^{I}_{D_x}} \\ \mathbf{f^{I}_{D_y}} \end{bmatrix} + \begin{bmatrix} \mathbf{f^{II}_{D_x}} \\ \mathbf{f^{II}_{D_y}} \end{bmatrix}, \tag{36}$$

where the vectors $\mathbf{f^{I}_{D_x}}$, $\mathbf{f^{I}_{D_y}}$ and $\mathbf{f^{II}_{D_x}}$, $\mathbf{f^{II}_{D_y}}$ represent the effects from the linear (37) and nonlinear drag forces (38), respectively:

$$\begin{bmatrix} \mathbf{f^{I}_{D_x}} \\ \mathbf{f^{I}_{D_y}} \end{bmatrix} = - \begin{bmatrix} c_t \mathbf{C}_\theta & -c_n \mathbf{S}_\theta \\ c_t \mathbf{S}_\theta & c_n \mathbf{C}_\theta \end{bmatrix} \begin{bmatrix} \mathbf{V_{r_x}} \\ \mathbf{V_{r_y}} \end{bmatrix}, \tag{37}$$

$$\begin{bmatrix} \mathbf{f^{II}_{D_x}} \\ \mathbf{f^{II}_{D_y}} \end{bmatrix} = - \begin{bmatrix} c_t \mathbf{C}_\theta & -c_n \mathbf{S}_\theta \\ c_t \mathbf{S}_\theta & c_n \mathbf{C}_\theta \end{bmatrix} \text{diag} \left(\text{sgn} \left(\begin{bmatrix} \mathbf{V_{r_x}} \\ \mathbf{V_{r_y}} \end{bmatrix} \right) \right) \begin{bmatrix} \mathbf{V^2_{r_x}} \\ \mathbf{V^2_{r_y}} \end{bmatrix}, \tag{38}$$

and where the relative velocities expressed in the body-fixed frame are given by

$$\begin{bmatrix} \mathbf{V_{r_x}} \\ \mathbf{V_{r_y}} \end{bmatrix} = \begin{bmatrix} \mathbf{C}_\theta & \mathbf{S}_\theta \\ -\mathbf{S}_\theta & \mathbf{C}_\theta \end{bmatrix} \begin{bmatrix} \dot{\mathbf{X}} - \mathbf{V}_x \\ \dot{\mathbf{Y}} - \mathbf{V}_y \end{bmatrix}. \tag{39}$$

Furthermore, $\mathbf{V}_x = \mathbf{e}V_x \in \mathbb{R}^N$ and $\mathbf{V}_y = \mathbf{e}V_y \in \mathbb{R}^N$, where V_x and V_y are the ocean current velocities in the inertial x- and y-direction, respectively, cf. Assumption 3.

The relative accelerations of the links in the body-fixed frame can be found by differentiating (39) with respect to time, which gives

$$\begin{aligned}\begin{bmatrix} \dot{\mathbf{V}}_{\mathbf{r_x}} \\ \dot{\mathbf{V}}_{\mathbf{r_y}} \end{bmatrix} &= \begin{bmatrix} \mathbf{C}_\theta & \mathbf{S}_\theta \\ -\mathbf{S}_\theta & \mathbf{C}_\theta \end{bmatrix} \begin{bmatrix} \ddot{\mathbf{X}} \\ \ddot{\mathbf{Y}} \end{bmatrix} \\ &+ \begin{bmatrix} -\mathbf{S}_\theta & \mathbf{C}_\theta \\ -\mathbf{C}_\theta & -\mathbf{S}_\theta \end{bmatrix} \begin{bmatrix} \mathrm{diag}(\dot{\boldsymbol{\theta}}) & \mathbf{0} \\ \mathbf{0} & \mathrm{diag}(\dot{\boldsymbol{\theta}}) \end{bmatrix} \begin{bmatrix} \dot{\mathbf{X}} - \mathbf{V}_x \\ \dot{\mathbf{Y}} - \mathbf{V}_y \end{bmatrix}.\end{aligned} \tag{40}$$

Following the procedure presented in Kelasidi et al., (2014a) and using the equation of the relative acceleration in body frame (40), the vectors $\mathbf{f}_{\mathbf{A_x}}$ and $\mathbf{f}_{\mathbf{A_y}}$ representing the added mass effects can be expressed as

$$\begin{bmatrix} \mathbf{f}_{\mathbf{A_x}} \\ \mathbf{f}_{\mathbf{A_y}} \end{bmatrix} = - \begin{bmatrix} \mathbf{C}_\theta & -\mathbf{S}_\theta \\ \mathbf{S}_\theta & \mathbf{C}_\theta \end{bmatrix} \begin{bmatrix} \mathbf{0} & \mathbf{0} \\ \mathbf{0} & \boldsymbol{\mu} \end{bmatrix} \begin{bmatrix} \dot{\mathbf{V}}_{\mathbf{r_x}} \\ \dot{\mathbf{V}}_{\mathbf{r_y}} \end{bmatrix}. \tag{41}$$

The parameter $\boldsymbol{\mu} = \mu_n \mathbf{I}_N$ represents the added mass of the fluid that is carried when the links move in their normal direction, cf. (34).

The **fluid torque** τ_i applied on link i by the fluid can be modeled as

$$\tau_i = -\tilde{\lambda}_1 \ddot{\theta}_i - \tilde{\lambda}_2 \dot{\theta}_i - \tilde{\lambda}_3 \mathrm{sgn}(\dot{\theta}_i) \dot{\theta}_i^2, \tag{42}$$

where the parameter $\tilde{\lambda}_1$ represents the added mass parameter, and the coefficients $\tilde{\lambda}_2$, $\tilde{\lambda}_3$ represent the drag torque parameters. These parameters depend on the shape of the body and the fluid characteristics.

Assembling the fluid torques acting on all links in matrix form, the fluid torques acting on all links are given by the vector

$$\boldsymbol{\tau} = -\boldsymbol{\Lambda}_1 \ddot{\boldsymbol{\theta}} - \boldsymbol{\Lambda}_2 \dot{\boldsymbol{\theta}} - \boldsymbol{\Lambda}_3 \mathrm{diag}\left(\mathrm{sgn}(\dot{\boldsymbol{\theta}})\right) \dot{\boldsymbol{\theta}}^2, \tag{43}$$

where $\boldsymbol{\Lambda}_1 = \tilde{\lambda}_1 \mathbf{I}_N$, $\boldsymbol{\Lambda}_2 = \tilde{\lambda}_2 \mathbf{I}_N$ and $\boldsymbol{\Lambda}_3 = \tilde{\lambda}_3 \mathbf{I}_N$.

2.4.2. The dynamics of the underwater snake robot (USR)

This section presents the resulting equations of motion for the underwater snake robot. In Kelasidi et al. (2014b,c, 2017b) it is shown that the force balance equation for all links of a USR can be expressed as

$$m\ddot{\mathbf{X}} = \mathbf{D^T h_x} + \mathbf{f_x}, \quad m\ddot{\mathbf{Y}} = \mathbf{D^T h_y} + \mathbf{f_y}. \tag{44}$$

Furthermore, the acceleration of the CM of the robot is given by

$$\begin{bmatrix} \ddot{p}_x \\ \ddot{p}_y \end{bmatrix} = \frac{1}{Nm} \begin{bmatrix} \mathbf{e}^T & \mathbf{0} \\ \mathbf{0} & \mathbf{e}^T \end{bmatrix} \begin{bmatrix} \mathbf{f_x} \\ \mathbf{f_y} \end{bmatrix}. \tag{45}$$

By first inserting (36) into (45), then inserting (41) into the resulting equation, thereafter inserting (40), and finally (18) and (21), we obtain the following equation for the acceleration of the CM of the robot:

$$\begin{aligned} \begin{bmatrix} \ddot{p}_x \\ \ddot{p}_y \end{bmatrix} &= -\mathbf{M_p N_p} \begin{bmatrix} \mathrm{diag}(\dot{\boldsymbol{\theta}}) & \mathbf{0} \\ \mathbf{0} & \mathrm{diag}(\dot{\boldsymbol{\theta}}) \end{bmatrix} \mathbf{E} \begin{bmatrix} \dot{p}_x \\ \dot{p}_y \end{bmatrix} \\ &- \mathbf{M_p N_p} \begin{bmatrix} \mathrm{diag}(\dot{\boldsymbol{\theta}}) & \mathbf{0} \\ \mathbf{0} & \mathrm{diag}(\dot{\boldsymbol{\theta}}) \end{bmatrix} \begin{bmatrix} l\mathbf{K}^T \mathbf{S}_\theta \dot{\boldsymbol{\theta}} - \mathbf{V}_x \\ -l\mathbf{K}^T \mathbf{C}_\theta \dot{\boldsymbol{\theta}} - \mathbf{V}_y \end{bmatrix} \\ &- \mathbf{M_p L_p} \begin{bmatrix} l\mathbf{K}^T (\mathbf{C}_\theta \dot{\boldsymbol{\theta}}^2 + \mathbf{S}_\theta \ddot{\boldsymbol{\theta}}) \\ l\mathbf{K}^T (\mathbf{S}_\theta \dot{\boldsymbol{\theta}}^2 - \mathbf{C}_\theta \ddot{\boldsymbol{\theta}}) \end{bmatrix} + \mathbf{M_p} \mathbf{E}^T \begin{bmatrix} \mathbf{f_{Dx}} \\ \mathbf{f_{Dy}} \end{bmatrix}, \end{aligned} \tag{46}$$

where $\mathbf{f_{Dx}} = \mathbf{f}^{\mathrm{I}}_{\mathbf{D_x}} + \mathbf{f}^{\mathrm{II}}_{\mathbf{D_x}}$ and $\mathbf{f_{Dy}} = \mathbf{f}^{\mathrm{I}}_{\mathbf{D_y}} + \mathbf{f}^{\mathrm{II}}_{\mathbf{D_y}}$, and the matrices $\mathbf{M_p}$, $\mathbf{N_p}$ and $\mathbf{L_p}$ are given by:

$$\mathbf{M_p} = \begin{bmatrix} m_{11} & m_{12} \\ m_{21} & m_{22} \end{bmatrix} = \begin{bmatrix} Nm + \mathbf{e}^T \mathbf{S}_\theta^2 \boldsymbol{\mu} \mathbf{e} & -\mathbf{e}^T \mathbf{S}_\theta \mathbf{C}_\theta \boldsymbol{\mu} \mathbf{e} \\ -\mathbf{e}^T \mathbf{S}_\theta \mathbf{C}_\theta \boldsymbol{\mu} \mathbf{e} & Nm + \mathbf{e}^T \mathbf{C}_\theta^2 \boldsymbol{\mu} \mathbf{e} \end{bmatrix}^{-1}, \tag{47}$$

$$\mathbf{N_p} = \begin{bmatrix} \mathbf{e}^T \mathbf{S}_\theta \mathbf{C}_\theta \boldsymbol{\mu} & \mathbf{e}^T \mathbf{S}_\theta^2 \boldsymbol{\mu} \\ -\mathbf{e}^T \mathbf{C}_\theta^2 \boldsymbol{\mu} & -\mathbf{e}^T \mathbf{S}_\theta \mathbf{C}_\theta \boldsymbol{\mu} \end{bmatrix}, \tag{48}$$

$$\mathbf{K} = \mathbf{A}^T \left(\mathbf{D}\mathbf{D}^T\right)^{-1} \mathbf{D}, \tag{49}$$

$$\mathbf{L_p} = \begin{bmatrix} \mathbf{e}^T \mathbf{S}_\theta^2 \boldsymbol{\mu} & -\mathbf{e}^T \mathbf{S}_\theta \mathbf{C}_\theta \boldsymbol{\mu} \\ -\mathbf{e}^T \mathbf{S}_\theta \mathbf{C}_\theta \boldsymbol{\mu} & \mathbf{e}^T \mathbf{C}_\theta^2 \boldsymbol{\mu} \end{bmatrix}. \tag{50}$$

Additionally, the torque balance equation is given by

$$\mathbf{J}\ddot{\boldsymbol{\theta}} = \mathbf{D}^T \mathbf{u} - l\mathbf{S}_\theta \mathbf{A}^T \mathbf{h_x} + l\mathbf{C}_\theta \mathbf{A}^T \mathbf{h_y} + \boldsymbol{\tau}, \tag{51}$$

where $\mathbf{J} = J\mathbf{I}_N$ and $\boldsymbol{\tau}$ is given by (43). The joint constraint forces can be obtained by multiplying (44) by $\mathbf{D}$ and solving for $\mathbf{h_x}$ and $\mathbf{h_y}$:

$$\begin{aligned} \mathbf{h_x} &= (\mathbf{D}\mathbf{D}^T)^{-1}\mathbf{D}(m\ddot{\mathbf{X}} - \mathbf{f_x}) \\ \mathbf{h_y} &= (\mathbf{D}\mathbf{D}^T)^{-1}\mathbf{D}(m\ddot{\mathbf{Y}} - \mathbf{f_y}). \end{aligned} \tag{52}$$

By inserting (52), (21) and (36) into (51), we get

$$\begin{aligned} &(\mathbf{J} + ml^2\mathbf{S}_\theta\mathbf{V}\mathbf{S}_\theta + ml^2\mathbf{C}_\theta\mathbf{V}\mathbf{C}_\theta)\ddot{\boldsymbol{\theta}} - (-ml^2\mathbf{S}_\theta\mathbf{V}\mathbf{C}_\theta + ml^2\mathbf{C}_\theta\mathbf{V}\mathbf{S}_\theta)\dot{\boldsymbol{\theta}}^2 \\ &= \mathbf{D}^T\mathbf{u} - ml\mathbf{S}_\theta\mathbf{K}\mathbf{e}\ddot{p}_x + ml\mathbf{C}_\theta\mathbf{K}\mathbf{e}\ddot{p}_y + l\mathbf{S}_\theta\mathbf{K}\mathbf{f_{Ax}} - l\mathbf{C}_\theta\mathbf{K}\mathbf{f_{Ay}} \\ &+ l\mathbf{S}_\theta\mathbf{K}\mathbf{f_{Dx}} - l\mathbf{C}_\theta\mathbf{K}\mathbf{f_{Dy}} + \boldsymbol{\tau}. \end{aligned} \tag{53}$$

Finally, by inserting (41), (46) and then (43) into (53), we are able to express the rotational equation of motion of the robot as follows:

$$\mathbf{M}_\theta\ddot{\boldsymbol{\theta}} + \mathbf{W}_\theta\dot{\boldsymbol{\theta}}^2 + \mathbf{V}_{\theta,\dot{\theta}}\dot{\boldsymbol{\theta}} + \mathbf{N}_{\theta,\dot{\theta}}(\mathbf{e}\dot{p}_x - \mathbf{V}_x) + \mathbf{P}_{\theta,\dot{\theta}}(\mathbf{e}\dot{p}_y - \mathbf{V}_y) + \mathbf{K_x}\mathbf{f_{Dx}} + \mathbf{K_y}\mathbf{f_{Dy}} = \mathbf{D}^T\mathbf{u}, \tag{54}$$

where $\mathbf{u} \in \mathbb{R}^{N-1}$ is the control input, and the matrices $\mathbf{M}_\theta$, $\mathbf{W}_\theta$, $\mathbf{V}_{\theta,\dot{\theta}}$, $\mathbf{N}_{\theta,\dot{\theta}}$ $\mathbf{P}_{\theta,\dot{\theta}}$, $\mathbf{K_x}$ and $\mathbf{K_y}$ are given by:

$$\begin{aligned} \mathbf{M}_\theta = \mathbf{J} &+ ml^2\mathbf{S}_\theta\mathbf{V}\mathbf{S}_\theta + ml^2\mathbf{C}_\theta\mathbf{V}\mathbf{C}_\theta - l\mathbf{S}_\theta\mathbf{K}\mathbf{A_1} + l\mathbf{C}_\theta\mathbf{K}\mathbf{A_4} + l\mathbf{K_5}\mathbf{K_1}\mathbf{K}^T\mathbf{S}_\theta \\ &- l\mathbf{K_5}\mathbf{K_2}\mathbf{K}^T\mathbf{C}_\theta + l\mathbf{K_6}\mathbf{K_3}\mathbf{K}^T\mathbf{S}_\theta + l\mathbf{K_6}\mathbf{K_4}\mathbf{K}^T\mathbf{C}_\theta + \boldsymbol{\Lambda}_1 \end{aligned} \tag{55}$$

$$\begin{aligned}\mathbf{W}_\theta = {} & ml^2\mathbf{S}_\theta\mathbf{V}\mathbf{C}_\theta - ml^2\mathbf{C}_\theta\mathbf{V}\mathbf{S}_\theta - l\mathbf{S}_\theta\mathbf{K}\mathbf{A_2} + l\mathbf{C}_\theta\mathbf{K}\mathbf{A_5} + l\mathbf{K_5}\mathbf{K_1}\mathbf{K}^T\mathbf{C}_\theta \\ & + l\mathbf{K_5}\mathbf{K_2}\mathbf{K}^T\mathbf{S}_\theta + l\mathbf{K_6}\mathbf{K_3}\mathbf{K}^T\mathbf{C}_\theta - l\mathbf{K_6}\mathbf{K_4}\mathbf{K}^T\mathbf{S}_\theta\end{aligned} \tag{56}$$

$$\begin{aligned}\mathbf{V}_{\theta,\dot\theta} = {} & -l\mathbf{S}_\theta\mathbf{K}\mathrm{diag}(\dot{\boldsymbol\theta})\mathbf{A_3} + l\mathbf{C}_\theta\mathbf{K}\mathrm{diag}(\dot{\boldsymbol\theta})\mathbf{A_6} - l\mathbf{K_5}\mathbf{K_2}\mathrm{diag}(\dot{\boldsymbol\theta})\mathbf{K}^T\mathbf{S}_\theta \\ & - l\mathbf{K_5}\mathbf{K_1}\mathrm{diag}(\dot{\boldsymbol\theta})\mathbf{K}^T\mathbf{C}_\theta + l\mathbf{K_6}\mathbf{K_4}\mathrm{diag}(\dot{\boldsymbol\theta})\mathbf{K}^T\mathbf{S}_\theta \\ & - l\mathbf{K_6}\mathbf{K_3}\mathrm{diag}(\dot{\boldsymbol\theta})\mathbf{K}^T\mathbf{C}_\theta + \boldsymbol\Lambda_2 + \boldsymbol\Lambda_3\mathrm{diag}(|\dot{\boldsymbol\theta}|)\end{aligned} \tag{57}$$

$$\mathbf{N}_{\theta,\dot\theta} = \left(l\mathbf{S}_\theta\mathbf{K}\mathbf{S}_\theta\mathbf{C}_\theta\boldsymbol\mu + l\mathbf{C}_\theta\mathbf{K}\mathbf{C}_\theta^2\boldsymbol\mu - \mathbf{K_5}\mathbf{K_2} + \mathbf{K_6}\mathbf{K_4}\right)\mathrm{diag}\,\dot{\boldsymbol\theta} \tag{58}$$

$$\mathbf{P}_{\theta,\dot\theta} = \left(l\mathbf{S}_\theta\mathbf{K}\mathbf{S}_\theta^2\boldsymbol\mu + l\mathbf{C}_\theta\mathbf{K}\mathbf{S}_\theta\mathbf{C}_\theta\boldsymbol\mu + \mathbf{K_5}\mathbf{K_1} + \mathbf{K_6}\mathbf{K_3}\right)\mathrm{diag}(\dot{\boldsymbol\theta}) \tag{59}$$

where

$$\mathbf{K_x} = -l\mathbf{S}_\theta\mathbf{K} - \mathbf{K_5}m_{11}\mathbf{e}^T - \mathbf{K_6}m_{21}\mathbf{e}^T,\ \mathbf{K_y} = l\mathbf{C}_\theta\mathbf{K} - \mathbf{K_5}m_{12}\mathbf{e}^T - \mathbf{Ks_6}m_{22}\mathbf{e}^T$$

$$\mathbf{A_1} = -l\mathbf{S}_\theta^2\boldsymbol\mu\mathbf{K}^T\mathbf{S}_\theta - l\mathbf{S}_\theta\mathbf{C}_\theta\boldsymbol\mu\mathbf{K}^T\mathbf{C}_\theta,\ \mathbf{A_2} = -l\mathbf{S}_\theta^2\boldsymbol\mu\mathbf{K}^T\mathbf{C}_\theta + l\mathbf{S}_\theta\mathbf{C}_\theta\boldsymbol\mu\mathbf{K}^T\mathbf{S}_\theta$$
$$\mathbf{A_3} = -l\mathbf{S}_\theta\mathbf{C}_\theta\boldsymbol\mu\mathbf{K}^T\mathbf{S}_\theta + l\mathbf{S}_\theta^2\boldsymbol\mu\mathbf{K}^T\mathbf{C}_\theta,\ \mathbf{A_4} = l\mathbf{S}_\theta\mathbf{C}_\theta\boldsymbol\mu\mathbf{K}^T\mathbf{S}_\theta + l\mathbf{C}_\theta^2\boldsymbol\mu\mathbf{K}^T\mathbf{C}_\theta$$
$$\mathbf{A_5} = l\mathbf{S}_\theta\mathbf{C}_\theta\boldsymbol\mu\mathbf{K}^T\mathbf{C}_\theta - l\mathbf{C}_\theta^2\boldsymbol\mu\mathbf{K}^T\mathbf{S}_\theta,\ \mathbf{A_6} = l\mathbf{C}_\theta^2\boldsymbol\mu\mathbf{K}^T\mathbf{S}_\theta - l\mathbf{S}_\theta\mathbf{C}_\theta\boldsymbol\mu\mathbf{K}^T\mathbf{C}_\theta$$

$$\mathbf{K_1} = m_{11}\mathbf{e}^T\mathbf{S}_\theta^2\boldsymbol\mu - m_{12}\mathbf{e}^T\mathbf{S}_\theta\mathbf{C}_\theta\boldsymbol\mu,\quad \mathbf{K_2} = -m_{11}\mathbf{e}^T\mathbf{S}_\theta\mathbf{C}_\theta\boldsymbol\mu + m_{12}\mathbf{e}^T\mathbf{C}_\theta^2\boldsymbol\mu$$
$$\mathbf{K_3} = m_{21}\mathbf{e}^T\mathbf{S}_\theta^2\boldsymbol\mu - m_{22}\mathbf{e}^T\mathbf{S}_\theta\mathbf{C}_\theta\boldsymbol\mu,\quad \mathbf{K_4} = m_{21}\mathbf{e}^T\mathbf{S}_\theta\mathbf{C}_\theta\boldsymbol\mu - m_{22}\mathbf{e}^T\mathbf{C}_\theta^2\boldsymbol\mu$$
$$\mathbf{K_5} = -ml\mathbf{S}_\theta\mathbf{K}\mathbf{e} - l\mathbf{S}_\theta\mathbf{K}\mathbf{S}_\theta^2\boldsymbol\mu\mathbf{e} - l\mathbf{C}_\theta\mathbf{K}\mathbf{S}_\theta\mathbf{C}_\theta\boldsymbol\mu\mathbf{e}$$
$$\mathbf{K_6} = ml\mathbf{C}_\theta\mathbf{K}\mathbf{e} + l\mathbf{S}_\theta\mathbf{K}\mathbf{S}_\theta\mathbf{C}_\theta\boldsymbol\mu\mathbf{e} + l\mathbf{C}_\theta\mathbf{K}\mathbf{C}_\theta^2\boldsymbol\mu\mathbf{e}$$

By defining the state variable $\mathbf{x} = \left[\boldsymbol\theta^T, \mathbf{p}_{\mathrm{CM}}^T, \dot{\boldsymbol\theta}^T, \dot{\mathbf{p}}_{\mathrm{CM}}^T\right]^T \in \mathbb{R}^{2N+4}$, we can rewrite the model of the robot compactly in state space form as

$$\dot{\mathbf{x}} = \left[\dot{\boldsymbol\theta}^T, \dot{\mathbf{p}}_{\mathrm{CM}}^T, \ddot{\boldsymbol\theta}^T, \ddot{\mathbf{p}}_{\mathrm{CM}}^T\right]^T = \mathbf{F}(\mathbf{x},\mathbf{u}), \tag{60}$$

where the elements of $\mathbf{F}(\mathbf{x},\mathbf{u})$ are found by solving (46) and (54) for $\ddot{\mathbf{p}}_{\mathrm{CM}}$ and $\ddot{\boldsymbol\theta}$, re-

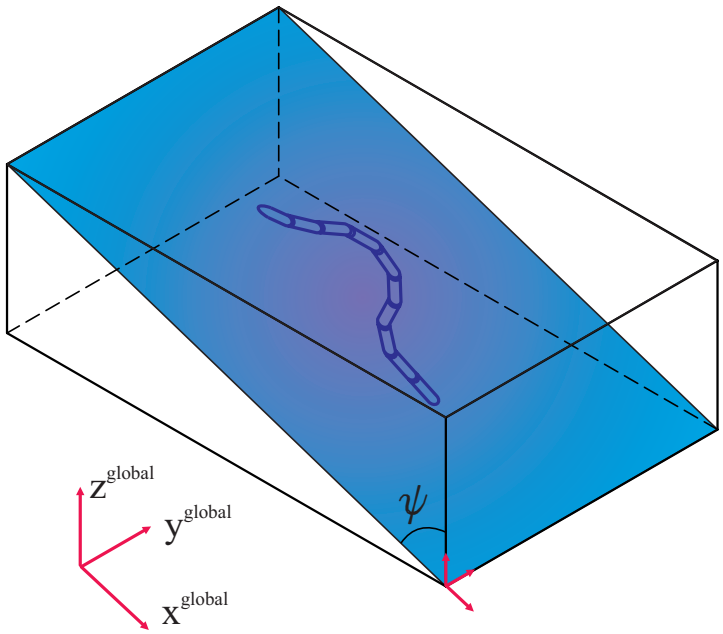

Figure 8: Visualization of a ten link underwater snake robot motion in any 2D tilted plane.

spectively.

Remark 5. *It is interesting to note that if we, in the dynamic model (46,54), set the fluid parameters equal to zero and replace the drag forces in the x- and y-direction with the ground friction forces from Section 2.3.1, then the model reduces exactly to the dynamic model of the snake robot moving on land described in Section 2.3.2. The underwater snake robot model is thus an extension of the land-based snake robot model and may be used for amphibious snake robots moving both on land and in water.*

The model can be extended to the case where the snake robot is not neutrally buoyant and moves in any 2D tilted plane, as shown in Fig. 8, including both the vertical and the horizontal plane. Please see Kelasidi et al. (2014a) for details.

Furthermore, the model can be extended to allow links of different mass and length, and to include various types of effectors along the snake robot body, like caudal, dorsal and pectoral fins, in addition to thrusters like tunnel thrusters and stern propellers Kelasidi et al. (2017b).

3. Analysis of locomotion: How to move forward

In this section we will see that if the friction or drag force coefficients are larger in the sideways (normal) direction than in the longitudinal (tangential) direction of the robot links, the snake robot can achieve forward propulsion by continuously changing its body shape to induce either ground friction forces or hydrodynamic drag forces that propel the robot forward. Biological snakes have this friction/drag property (Bauchot (1994)).

3.1. Controllability with isotropic friction or drag forces

We begin by analyzing the controllability of the snake robot when the ground friction forces, or drag forces when moving underwater, are isotropic, i.e. $c_t = c_n = c$ in (27) and (37)-(38).

Theorem 1. *Consider the snake robots described in Section 2.*

- *A snake robot moving on a flat horizontal plane, influenced by* isotropic *viscous ground friction, is not controllable.*
- *A snake robot moving in a virtual horizontal plane underwater, influenced by* isotropic *drag forces, and with negligible added mass and non-linear drag effects, is not controllable.*

Proof. A nonlinear system is called controllable if there exist admissible control inputs that will move the system between two arbitrary states in finite time (Nijmeijer and Schaft (1990)). When $c_t = c_n$ the equations of motion take on a particularly simple form that enables us to study controllability through inspection of the equations of motion. First, consider the case when the snake robot moves on land. From (28b), the acceleration of the CM of the snake robot moving on land is given as

$$\begin{bmatrix} \ddot{p}_x \\ \ddot{p}_y \end{bmatrix} = \frac{1}{Nm} \begin{bmatrix} \mathbf{e}^T \mathbf{f}_{R,x} \\ \mathbf{e}^T \mathbf{f}_{R,y} \end{bmatrix} = \frac{1}{Nm} \begin{bmatrix} \sum_{i=1}^{N} \mathbf{f}_{R,x,i} \\ \sum_{i=1}^{N} \mathbf{f}_{R,y,i} \end{bmatrix}. \tag{61}$$

By inserting (22) into (61), the CM acceleration of the robot is given as

$$\begin{bmatrix} \ddot{p}_x \\ \ddot{p}_y \end{bmatrix} = \frac{c}{Nm} \begin{bmatrix} -N\dot{p}_x + \left(\sum_{i=1}^{N} \boldsymbol{\sigma}_i\right) \mathbf{S}_\theta \dot{\theta} \\ -N\dot{p}_y - \left(\sum_{i=1}^{N} \boldsymbol{\sigma}_i\right) \mathbf{C}_\theta \dot{\theta} \end{bmatrix} = -\frac{c}{m} \begin{bmatrix} \dot{p}_x \\ \dot{p}_y \end{bmatrix}, \tag{62}$$

because it can be shown that $\sum_{i=1}^{N} \boldsymbol{\sigma}_i = \mathbf{0}$.

To control the position, the snake robot must accelerate its CM. From (62), it is clear that the CM acceleration is proportional to the CM velocity. If the robot starts from rest ($\dot{\mathbf{p}}_{\mathbf{CM}} = \mathbf{0}$), it is therefore impossible to achieve acceleration of the CM. The position of the robot is in other words uncontrollable in this case.

When the snake robot moves underwater, under the assumption that the added mass and non-linear drag effects are negligible, the acceleration of the CM is given by

$$\begin{bmatrix} \ddot{p}_x \\ \ddot{p}_y \end{bmatrix} = \frac{1}{Nm} \begin{bmatrix} \mathbf{e}^T \mathbf{f}^{\mathrm{I}}_{\mathbf{D_x}} \\ \mathbf{e}^T \mathbf{f}^{\mathrm{I}}_{\mathbf{D_y}} \end{bmatrix}, \tag{63}$$

with the drag forces given by (37):

$$\begin{bmatrix} \mathbf{f}^{\mathrm{I}}_{\mathbf{D_x}} \\ \mathbf{f}^{\mathrm{I}}_{\mathbf{D_y}} \end{bmatrix} = - \begin{bmatrix} c_t \mathbf{C}_\theta & -c_n \mathbf{S}_\theta \\ c_t \mathbf{S}_\theta & c_n \mathbf{C}_\theta \end{bmatrix} \begin{bmatrix} \mathbf{V}_{\mathbf{r_x}} \\ \mathbf{V}_{\mathbf{r_y}} \end{bmatrix}. \tag{64}$$

By using (39) and then (18), and that the drag forces are isotropic, i.e. $c_n = c_t = c$, we find that

$$\begin{bmatrix} \ddot{p}_x \\ \ddot{p}_y \end{bmatrix} = \frac{c}{Nm} \begin{bmatrix} -N(\dot{p}_x - V_x) - \mathbf{e}^T l \mathbf{K}^T \mathbf{S}_\theta \dot{\boldsymbol{\theta}} \\ -N(\dot{p}_y - V_y) + \mathbf{e}^T l \mathbf{K}^T \mathbf{C}_\theta \dot{\boldsymbol{\theta}} \end{bmatrix}. \tag{65}$$

By manually investigating the structure of each row, cf. (19), and again using that $\sum_{i=1}^{N} \boldsymbol{\sigma}_i = \mathbf{0}$, we then have that

$$\begin{bmatrix} \ddot{p}_x \\ \ddot{p}_y \end{bmatrix} = -\frac{c}{m} \begin{bmatrix} \dot{p}_x - V_x \\ \dot{p}_y - V_y \end{bmatrix}. \tag{66}$$

We see that if the velocity of the robot's CM equals the ocean current velocity, i.e. if the robot drifts along with the current, then the right-hand side is zero and it is impossible to achieve an acceleration of the CM. Consequently there exist no admissible control inputs that will move the system from this state to an arbitrary other state, and the system is thus not controllable. □

Remark 6. *Negligible added mass effects is a common assumption for slowly moving underwater vehicles (Fossen (2011)). In particular, it is an assumption that is frequently made for bio-inspired robots (Colgate and Lynch (2004); McIsaac and Ostrowski (2003); Wang et al. (2013)). Furthermore, the quadratic terms of the nonlinear drag effects will be negligible for slowly moving robots.*

Remark 7. *The result agrees with studies of aquatic swimming animals. These have shown that there are three dominant mechanisms that are responsible for the propulsion of aquatic animals: drag forces, added mass forces and forces due to lift effects. Furthermore, it is shown that the drag forces are dominant for the anguilliform swimmers, i.e. for flexible elongate aquatic animals like snakes and eels (Sfakiotakis et al. (1999)).*

Theorem 1 is an extended version of (Liljebäck et al., 2013, Theorem 4.4).

3.2. Propulsive forces with anisotropic friction and drag

In Section 3.1 we saw that anisotropic ground friction forces are necessary for controllability when the snake robot moves on land. Furthermore, we found that when the snake robot swims underwater, something which will entail relatively low velocities such that added mass and higher-order drag effects are negligible, we need anisotropic drag forces in order to efficiently control the snake robot.

Snake robots should, therefore, be designed such that they have this anisotropic friction/drag property. For snake robots moving on land, this can be achieved by equipping each link of the robot with passive wheels, or mounting edges, or grooves, that run parallel to each link on the underside of each link (see e.g. Saito et al. (2002)). For snake robots moving in water, on the other hand, the robot can have a completely

smooth outer surface, and it will still have this anisotropic drag property due to its prolonged shape which produces higher drag forces in the direction normal to each link compared to in the tangential link direction (see e.g. Boyer et al. (2006b); McIsaac and Ostrowski (2003)).

In the following, we will analyze the forces acting in the forward direction of the snake robot, to identify how and why anisotropic friction/drag provides propulsive forces. Without loss of generality, we assume that global coordinate system is positioned such that the forward direction of motion is along the global positive x-axis, i.e. such that $|\theta_i| < \pi/2$, $\forall i \in [1,N]$. From (28b) and (27), we find that the total force acting on the snake robot in the forward direction when moving on land is

$$F_{\text{prop}} = Nm\ddot{p}_x = \mathbf{e}^T \mathbf{f}_{R,x} = -\mathbf{e}^T \Big(\Big(c_t (\mathbf{C}_\theta)^2 + c_n (\mathbf{S}_\theta)^2 \Big) \dot{\mathbf{X}} + (c_t - c_n) \mathbf{S}_\theta \mathbf{C}_\theta \dot{\mathbf{Y}} \Big) \tag{67}$$

i.e.

$$F_{\text{prop}} = -\sum_{i=1}^{N} F_x(\theta_i)\, \dot{x}_i - \sum_{i=1}^{N} F_y(\theta_i)\, \dot{y}_i, \tag{68}$$

where

$$F_x(\theta_i) = c_t \cos^2 \theta_i + c_n \sin^2 \theta_i, \tag{69}$$

$$F_y(\theta_i) = (c_t - c_n) \sin \theta_i \cos \theta_i, \tag{70}$$

and where we recall from Section 2.2 that the angle θ_i of link i is expressed with respect to the global x-axis, cf. Fig. 9. We see from (68) that F_{prop} consists of two components, one involving the linear velocity of each link in the *forward* direction of motion, $F_x(\theta_i)\dot{x}_i$, and one involving the linear velocity *normal* to the direction of motion, $F_y(\theta_i)\dot{y}_i$. Due to the negative signs in (68), the products $F_x(\theta_i)\dot{x}_i$ and $F_y(\theta_i)\dot{y}_i$ provide a positive contribution to the propulsive force only if they are *negative*. Since the friction coefficients, c_t and c_n, are always positive, the expression $F_x(\theta_i)$ given by (69), is obviously always positive. We assume that the snake robot motion does not involve x-direction velocity opposite to the direction of motion for any of the links. When the snake robot moves in the forward direction ($\dot{p}_x > 0$) we, therefore, have that

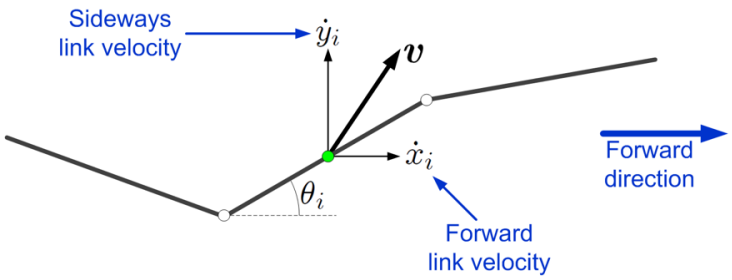

Figure 9: Kinematic variables the in forward and sideways direction of the snake robot

$\dot{x}_i > 0$, which means that the product $F_x(\theta_i)\dot{x}_i$ of the propulsive force is always positive. This product is, therefore, *not* contributing to the forward propulsion of the robot, but rather opposing it. This is as expected since the friction acts in the opposite direction of the direction of motion.

Any propulsive force in the forward direction of motion must, therefore, be produced by the *sideways* motion of the links, i.e. the product $F_y(\theta_i)\dot{y}_i$. We see from (70) that if $c_n = c_t$, then $F_y(\theta_i) = 0$, and consequently there exist no propulsive forces driving the snake robot forward, which complies with the controllability result in Theorem 1. However, when $c_n > c_t$, it can be seen from (70) that $F_y(\theta_i)\dot{y}_i$ is negative (the sideways motion of link i contributes to the propulsion) as long as $\operatorname{sgn}(\theta_i) = \operatorname{sgn}(\dot{y}_i)$ (Liljebäck et al. (2013)). This is achieved when the snake robot moves according to an undulatory motion pattern, which will be discussed in Section 3.3. The above analysis can be summarized in the following theorem and property (see Liljebäck et al. (2013) for further details):

Theorem 2. *Consider snake robots that move on land, described by (30). If $c_n > c_t$, sideways motion of link i contributes to the propulsion of the snake robot if* $\operatorname{sgn}(\theta_i) = \operatorname{sgn}(\dot{y}_i)$.

Property 1. *For a snake robot described by (30) with $c_n > c_t$, the magnitude of the propulsive force produced by link i, $\left|F_{\text{prop},i}\right|$, is increased by increasing the ratio $\frac{c_n}{c_t}$, or by increasing the magnitude of the sideways link velocity, $|\dot{y}_i|$, or by increasing $|\theta_i|$ as long as $|\theta_i| < 45°$.*

For underwater snake robots, it is not straightforward to obtain results that are anal-

ogous to Theorem 2, because added mass effects, nonlinear drag, and ocean currents complicate the structure of (68) significantly. However, with additional assumptions regarding the gait pattern, it is possible to obtain a similar result, as will be shown in the next section.

3.3. Undulatory locomotion

We have seen in Section 3.2 that if the snake robot moving on land has the anisotropic friction property $c_n > c_t$, then propulsive forces driving the snake robot forward are generated if $\operatorname{sgn}(\theta_i) = \operatorname{sgn}(\dot{y}_i)$. This is achieved when the snake robot follows an undulatory gait pattern Liljebäck et al. (2013). An undulatory gait pattern can be generated by requiring each link angle, ϕ_i, $i \in \{1,\dots,N-1\}$, to follow the reference signal

$$\phi_{i,\mathrm{ref}}(t) = \alpha g(i,N)\sin(\omega t + (i-1)\delta) + \phi_0, \tag{71}$$

where α is the maximum amplitude, ω is the frequency, δ is the phase shift between adjacent joints, and ϕ_0 is a constant offset that induces turning motion Saito et al. (2002). The function $g : \mathbb{R} \mapsto [0,1]$ scales the amplitude of the joints. For instance, $g(i,N) = 1$ gives the motion pattern lateral undulation, while $g(i,N) = \frac{N-i}{N+1}$ gives eel-like motion Kelasidi et al. (2014b).

In Liljebäck et al. (2013) it is shown that anisotropic ground friction gives the robot the controllability property *locally strongly accessible* from any equilibrium point, except from certain singular configurations. These singular configurations are shapes where all the relative joint angles are equal, i.e. $\phi_1 = \cdots = \phi_{N-1}$. This supports including the phase shift δ in the undulatory motion pattern (71).

The gait pattern (71) has the property that the sign condition of Theorem 2 always holds. It was furthermore shown in Kohl et al. (2015a) that it has an additional important property for underwater robots: the sign of the force components due to added mass and the current component in the y-direction alternate along the body. This means that when taking the sum of the forces that act on all links, these terms will cancel each other, except for a small remainder that can be treated as a disturbance. If the gait has certain symmetry properties, they will even be canceled completely. Furthermore, the

gait pattern (71) leads to slow motion, which is why non-linear drag effects do not significantly contribute to the propulsion. This is summarized in the following theorem which states that the undulatory gait pattern (71) gives forward propulsion when the snake robot moves underwater if the drag coefficients satisfy $c_n > c_t$ (see Kohl et al. (2015a) for further details):

Theorem 3. *Consider underwater snake robots, described by (60). If $c_n > c_t$ then the undulatory gait pattern* (71) *gives a sideways motion of link i that contributes to the propulsion of the snake robot. Furthermore, the ocean current contributes to propulsion if it has a positive x-component, while it opposes propulsion if the x-component is negative.*

4. The control-oriented model: Modeling undulatory locomotion

The mathematical models from Section 2 are complex, and we will in this section show that an observation about the nature of undulatory locomotion allows us to develop simpler models. These models capture the essential behavior of snake robots during undulatory locomotion and are well-suited for analysis and control design.

In Section 3.2 we saw that it is the sideways motion (transversal to the direction of motion of the robot) of each link that makes the snake robot move forward, something which is obtained by an undulatory motion pattern. In particular, lateral undulation mainly consists of link displacements that are transversal to the direction of motion (Liljebäck et al., 2013, Property 4.8). So during undulatory motion, it is the sideways motion of each link that produces propulsion. This insight motivates us to model the sideways motion of each link instead of the rotational motion of each joint. In this way, we capture the essential behavior of the robot, which is its propulsion, when designing controllers for path following.

Modeling the transversal link displacements instead of the rotational joint motion, corresponds to modeling the snake robot as a series of prismatic (translational) joints instead of revolute joints, see Fig. 10. Correspondingly, we now define the sideways displacement of the center of mass of each link as new state variables.

Assumption 5. *The snake robot moves using an undulatory gait pattern.*

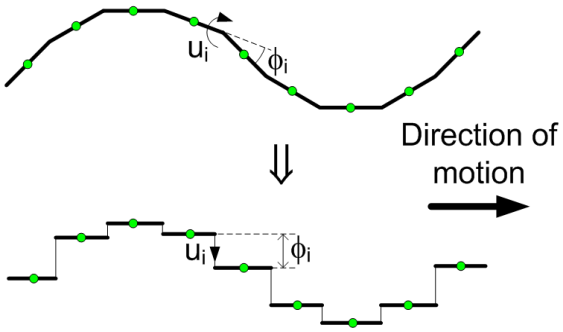

Figure 10: The snake robot is modeled as a series of prismatic joints that displace the CM of each link transversal to the direction of motion.

Assumption 6. *The joint angles of the snake robot are assumed to be small, and the joints can thus be modeled as prismatic joints.*

Remark 8. *Assumption 6 is a valid assumption for all joint angles* $\phi_i < 45\,\text{deg}$*, and the smaller the joint angles are, the better is the accuracy of the approximation.*

Remark 9. *Note that the control-oriented models presented in this section are* not *intended as accurate simulation models of snake robot locomotion. The models are intentionally based on the simplifying Assumption 6 to capture the essential dynamics of the robot during undulatory locomotion, to arrive at equations of motion that are well-suited for control design and stability analysis purposes. To this end, the model only needs to be* qualitatively *similar to the mathematical models in Section 2.*

Furthermore, to ensure that an undulatory gait pattern leads to propulsion, the following assumption must be made, as seen in Section 3:

Assumption 7. *The friction/drag coefficients satisfy* $c_n > c_t$.

4.1. Notations

When describing the kinematics and dynamics of the control-oriented model, we will use the mathematical symbols outlined in Table 2 and illustrated in Fig. 11 and Fig. 12.

In addition to notation defined in Section 2.1, we define the summation vector $\overline{\mathbf{e}} = [1,\ldots,1]^T \in \mathbb{R}^{N-1}$ for adding all elements of $(N-1)$-dimensional vectors, and

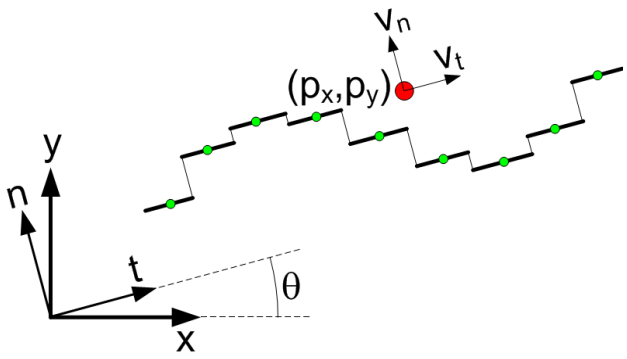

Figure 11: Illustration of the two coordinate frames employed in the control-oriented model. The global *x*-*y* frame is fixed. The *t*-*n* frame is always aligned with the snake robot.

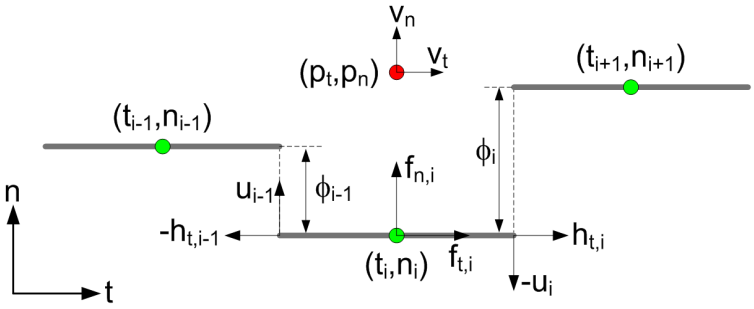

Figure 12: Parameters characterizing the kinematics and dynamics of the snake robot.

Table 2: Parameters that characterize the snake robot.

Symbol	Description
N	Number of links.
l	Length of a link.
m	Mass of each link.
ϕ_i	Normal direction distance between links i and $i+1$.
$v_{\phi,i}$	Relative velocity between links i and $i+1$.
θ	Orientation of the snake robot.
v_θ	Angular velocity of the snake robot.
(t_i, n_i)	Coordinates of the CM of link i in the t-n frame.
(p_t, p_n)	Coordinates of the CM of the robot in the t-n frame.
(p_x, p_y)	Coordinates of the CM of the robot in the global frame.
(v_t, v_n)	Forward and normal direction velocity of the robot.
u_i	Actuator force at joint i.
$(f_{R,x,i}, f_{R,y,i})$	Friction force on link i in the global frame.
$(f_{t,i}, f_{n,i})$	Friction force on link i in the t-n frame.

the matrix $\overline{\mathbf{D}} = \mathbf{D}^T \left(\mathbf{D}\mathbf{D}^T\right)^{-1} \in \mathbb{R}^{N\times(N-1)}$.

We consider a planar snake robot with N links of length l interconnected by $N-1$ motorized *prismatic* (translational) joints. Note that we denote the total link length in the control-oriented model by l, whereas the total link length in the model in Section 2 was $2l$ for notational convenience.

We define the motion of the robot with respect to the two coordinate frames illustrated in Fig. 11. The x-y frame is the fixed global frame. The t-n frame is always aligned with the snake robot, i.e. the t- and n-axis always point in the *tangential* and *normal* direction of the robot, respectively. The origin of both frames are fixed and coincide. We will denote the direction of the t-axis as the *tangential* or *forward* direction of the robot, and the direction of the n-axis as the *normal* direction. Note that we do not refer to the t-n frame as the *body* frame of the snake robot since the t-n frame is not fixed to the robot. However, if a body frame fixed to the robot had been defined, the orientation of this frame would be identical to the orientation of the t-n frame.

The position of the snake robot is described through the coordinates of its center

of mass. As seen in Fig. 11 and Fig. 12, the global frame position of the robot is denoted by $(p_x, p_y) \in \mathbb{R}^2$, while the t-n frame position is denoted by $(p_t, p_n) \in \mathbb{R}^2$. The global frame orientation of the robot is denoted by $\theta \in \mathbb{R}$ and is expressed with respect to the global x axis. The angle between the global x-axis and the t-axis is also θ since the t-n frame is always aligned with the robot. Describing the position in a frame which is always aligned with the snake robot is inspired by and similar to a coordinate transformation proposed in Pettersen and Egeland (1996).

We denote the t-n frame position of the CM of link i by $(t_i, n_i) \in \mathbb{R}^2$. The $N-1$ prismatic joints of the snake robot control the normal direction distance between the links. As seen in Fig. 12, the normal direction distance between link i and link $i+1$ is given by

$$\phi_i = n_{i+1} - n_i, \tag{72}$$

and represents the coordinate of joint i. The controlled distance ϕ_i replaces the controlled joint angle in the original model from Section 2.2

Remark 10. *The state ϕ_i of joint i in the control-oriented model is a translational* distance*, while the state ϕ_i of joint i in the model in Section 2 is a joint* angle*. In the control-oriented model we, therefore, refer to ϕ_i as a joint coordinate instead of a joint angle.*

4.2. The kinematics and dynamics of the snake robot moving on land

In (Liljebäck et al., 2013, Chapter 6) it is shown that under Assumptions 5–7 the control-oriented kinematics and dynamics of snake robots moving on land with viscous

friction can be written

$$\dot{\boldsymbol{\phi}} = \mathbf{v}_\phi, \tag{73a}$$

$$\dot{\theta} = v_\theta, \tag{73b}$$

$$\dot{p}_x = v_t \cos\theta - v_n \sin\theta, \tag{73c}$$

$$\dot{p}_y = v_t \sin\theta + v_n \cos\theta, \tag{73d}$$

$$\dot{\mathbf{v}}_\phi = -\frac{c_n}{m}\mathbf{v}_\phi + \frac{c_p}{m} v_t \mathbf{A}\mathbf{D}^T \boldsymbol{\phi} + \frac{1}{m}\mathbf{D}\mathbf{D}^T \mathbf{u}, \tag{73e}$$

$$\dot{v}_\theta = -\lambda_1 v_\theta + \frac{\lambda_2}{N-1} v_t \bar{\mathbf{e}}^T \boldsymbol{\phi}, \tag{73f}$$

$$\dot{v}_t = -\frac{c_t}{m} v_t + \frac{2c_p}{Nm} v_n \bar{\mathbf{e}}^T \boldsymbol{\phi} - \frac{c_p}{Nm} \boldsymbol{\phi}^T \mathbf{A}\overline{\mathbf{D}} \mathbf{v}_\phi, \tag{73g}$$

$$\dot{v}_n = -\frac{c_n}{m} v_n + \frac{2c_p}{Nm} v_t \bar{\mathbf{e}}^T \boldsymbol{\phi}, \tag{73h}$$

where $\mathbf{u} \in \mathbb{R}^{N-1}$ are the actuator forces at the joints, $\mathbf{A}$, $\mathbf{D}$, $\overline{\mathbf{D}}$, and $\bar{\mathbf{e}}$ are defined in Section 2.1 and at the beginning of Section 4, c_t and c_n correspond, respectively, to the tangential and normal direction friction coefficient of the links in the mathematical model of the snake robot in Section 2.3, $c_p = \frac{c_n - c_t}{2l}$, and λ_1 and λ_2 are positive scalar constants which characterize the rotational motion of the snake robot.

We choose the state vector of the system as

$$\mathbf{x} = \left[\boldsymbol{\phi}^T, \theta, p_x, p_y, \mathbf{v}_\phi^T, v_\theta, v_t, v_n\right]^T \in \mathbb{R}^{2N+4}, \tag{74}$$

where $\boldsymbol{\phi} \in \mathbb{R}^{N-1}$ are the joint coordinates, $\theta \in \mathbb{R}$ is the absolute orientation, $(p_x, p_y) \in \mathbb{R}^2$ is the global frame position of the CM, $\mathbf{v}_\phi = \dot{\boldsymbol{\phi}} \in \mathbb{R}^{N-1}$ are the joint velocities, $v_\theta = \dot{\theta} \in \mathbb{R}$ is the angular velocity, and v_t and v_n are the tangential and normal direction velocity of the snake robot, respectively.

Similar to the partial feedback linearization performed for the model in Section 2, we will usually assume that the actuator forces of the control-oriented model are set according to the linearizing control law

$$\mathbf{u} = m\left(\mathbf{D}\mathbf{D}^T\right)^{-1}\left(\bar{\mathbf{u}} + \frac{c_n}{m}\dot{\boldsymbol{\phi}} - \frac{c_p}{m} v_t \mathbf{A}\mathbf{D}^T \boldsymbol{\phi}\right), \tag{75}$$

where $\overline{\mathbf{u}} = [\overline{u}_1, \ldots, \overline{u}_{N-1}]^T \in \mathbb{R}^{N-1}$ is a new set of control inputs. This control law transforms the joint dynamics (73e) into

$$\dot{\mathbf{v}}_\phi = \overline{\mathbf{u}}. \tag{76}$$

4.3. The kinematics and dynamics of the snake robot moving underwater

For the control-oriented model, higher order damping terms will be disregarded since these higher order nonlinearities complicate the analysis and corresponding control design, and at the same time they are helpful, stabilizing terms during locomotion. We would therefore not want to cancel these out through control design, but rather keep their stabilizing effect. Furthermore, the velocity of the robot during undulatory locomotion is relatively low, especially for small link angles, which also makes the linear drag forces dominate the higher order drag forces. We, therefore, make the following assumption:

Assumption 8. *The nonlinear drag forces* (38) *are negligible during undulatory locomotion.*

Furthermore, since the snake robot moves relatively slowly during undulatory locomotion, as discussed in Section 3.1, Remark 6, it is a valid assumption that the added mass effects are negligible. This assumption further simplifies the control-oriented model, while capturing the effects that are significant for control design.

Assumption 9. *The added mass effects are negligible during undulatory locomotion.*

The kinematics and dynamics of swimming snake robots that satisfy Assumptions 1-9 can be described by the control-oriented model (Kohl et al. (2015b))

$$\dot{\boldsymbol{\phi}} = \mathbf{v}_\phi, \tag{77a}$$

$$\dot{\theta} = v_\theta, \tag{77b}$$

$$\dot{p}_x = v_t \cos\theta - v_n \sin\theta, \tag{77c}$$

$$\dot{p}_y = v_t \sin\theta + v_n \cos\theta, \tag{77d}$$

$$\dot{\mathbf{v}}_\phi = -\frac{c_n}{m}\mathbf{v}_\phi + \frac{c_p}{m} v_{t,\mathrm{rel}} \mathbf{A}\mathbf{D}^T \boldsymbol{\phi} + \frac{1}{m}\mathbf{D}\mathbf{D}^T \mathbf{u}, \tag{77e}$$

$$\dot{v}_\theta = -\lambda_1 v_\theta + \frac{\lambda_2}{N-1} v_{t,\mathrm{rel}} \bar{\mathbf{e}}^T \boldsymbol{\phi}, \tag{77f}$$

$$\dot{v}_t = -\frac{c_t}{m} v_{t,\mathrm{rel}} + \frac{2c_p}{Nm} v_{n,\mathrm{rel}} \bar{\mathbf{e}}^T \boldsymbol{\phi} - \frac{c_p}{Nm} \boldsymbol{\phi}^T \mathbf{A}\overline{\mathbf{D}}\mathbf{v}_\phi, \tag{77g}$$

$$\dot{v}_n = -\frac{c_n}{m} v_{n,\mathrm{rel}} + \frac{2c_p}{Nm} v_{t,\mathrm{rel}} \bar{\mathbf{e}}^T \boldsymbol{\phi}, \tag{77h}$$

The ocean current disturbance enters the above equations through $v_{t,\mathrm{rel}}$ and $v_{n,\mathrm{rel}}$, which are the relative velocities in the body-aligned frame. They are obtained by

$$\begin{bmatrix} v_{t,\mathrm{rel}} \\ v_{n,\mathrm{rel}} \end{bmatrix} = \begin{bmatrix} v_t \\ v_n \end{bmatrix} - \begin{bmatrix} V_t \\ V_n \end{bmatrix}, \tag{78}$$

where V_t and V_n denote the ocean current velocities in the body-aligned frame, i.e.

$$\begin{bmatrix} V_t \\ V_n \end{bmatrix} = \begin{bmatrix} \cos\theta & \sin\theta \\ -\sin\theta & \cos\theta \end{bmatrix} \begin{bmatrix} V_x \\ V_y \end{bmatrix}, \tag{79}$$

where V_x and V_y are given by Assumption 3.

We see that the structure of this model is the same as for the snake robot moving on land (73). The friction coefficients when moving on land play the same role as the drag parameters when moving underwater. The additional feature of (77) is that it takes into account the disturbances from ocean currents.

It is verified by analysis and experiments in (Liljebäck et al., 2013, Chapter 6), Kohl et al. (2015b) and Kohl et al. (2017) that the control-oriented models (73) and (77) are

valid representations of the snake robot dynamics for motion on land and underwater, respectively, when the joint angles are small.

5. How to choose the gait pattern parameters for undulatory locomotion

From Section 3 we know that under Assumption 7 the undulatory gait pattern generated by the reference signal (71):

$$\phi_{i,\mathrm{ref}}(t) = \alpha g(i,N)\sin\left(\omega t + (i-1)\delta\right) + \phi_0,$$

will make the snake robot move forward. In this section we address the question of how to choose the gait parameters α, ω and δ. In particular, we want to understand the relationship between these gait parameters and the forward velocity.

5.1. Relationship between the gait parameters and the forward velocity

The joint motion following (71) is time-periodic, and this suggests that there is some average effect of the joint motion that propels the robot forward. We, therefore, use averaging theory Sanders et al. (2007) to study the average effect of the joint motion during undulatory locomotion, applied to the control-oriented models from Section 4. This analysis reveals properties of undulatory snake robot locomotion that are both fundamental and useful from a motion planning perspective. In particular, we see that the average velocity of a snake robot during undulatory locomotion converges exponentially fast to a steady-state velocity, and an analytical expression is given for calculating this steady-state velocity as a function of the gait pattern parameters.

5.1.1. Snake robots moving on land

In this section, we consider snake robots that move on land using lateral undulation, i.e. according to the reference signal (71) with $g(i,N) = 1$:

$$\phi_{i,\mathrm{ref}}(t) = \alpha\sin\left(\omega t + (i-1)\delta\right) + \phi_0, \tag{80}$$

We assume that the joint offset ϕ_0 is constant so that

$$\begin{aligned}\dot{\phi}_{i,\mathrm{ref}}(t) &= \alpha g(i,N)\omega\cos(\omega t+(i-1)\delta),\\ \ddot{\phi}_{i,\mathrm{ref}}(t) &= -\alpha g(i,N)\omega^2\sin(\omega t+(i-1)\delta),\end{aligned} \tag{81}$$

It is shown in (Liljebäck et al., 2013, Chapter 7) that under the condition that (please note that there was a typo in the original expression):

$$|\phi_0| < \tfrac{N}{2(N-1)}\tfrac{\sqrt{c_n c_t}}{c_p}, \tag{82}$$

the average velocity, $\mathbf{v}_{av}$, will converge exponentially to the steady state velocity

$$\mathbf{v}^* = \alpha^2\omega k_\delta \begin{bmatrix} \frac{Nc_nc_p}{2(c_nc_tN^2-4(N-1)^2c_p^2\phi_0^2)} \\ \frac{c_p^2\phi_0(N-1)}{c_nc_tN^2-4(N-1)^2c_p^2\phi_0^2} \\ \frac{Nc_nc_p\lambda_2\phi_0}{2\lambda_1(c_nc_tN^2-4(N-1)^2c_p^2\phi_0^2)} \end{bmatrix}. \tag{83}$$

Averaging theory gives that for sufficiently large frequencies ω, the average velocity of the snake robot will approximate the exact velocity $\mathbf{v} = [v_t \; v_n \; v_\theta]^T$ given by (73f), (73g), and (73h). This is summarized in the following theorem (see Liljebäck et al. (2013) for further details):

Theorem 4. *Consider a snake robot described by (73). Suppose the joint coordinates $\boldsymbol{\phi}$ are controlled in exact accordance with (80) and (81), and that the joint coordinate offset ϕ_o satisfies (82). Then there exist $k > 0$ and $\omega^* > 0$ such that for all $\omega > \omega^*$,*

$$\|\mathbf{v}(t) - \mathbf{v}_{av}(t)\| \leq \tfrac{k}{\omega} \quad \textit{for all } t \in [0,\infty), \tag{84}$$

Furthermore, the average velocity $\mathbf{v}_{av}(t)$ of the snake robot will converge exponentially fast to the steady state velocity $\mathbf{v}^*$ given by (83).

Theorem 4 is a powerful result. First of all, it proves mathematically that lateral undulation enables a snake robot with anisotropic ground friction properties to achieve forward propulsion (under the assumption that the body shape motion is modeled as translational link displacements). Second, the result gives an analytical expression for

the steady state velocity as a function of the controller parameters α, ω, δ, and ϕ_o, i.e. the amplitude, frequency, phase shift and offset of the joint motion during lateral undulation. This information is relevant for motion planning purposes. We can for example immediately see from (83) that the steady state velocity of the snake robot when it conducts lateral undulation with zero joint offset ($\phi_o = 0$) is given by $v_t^* = \frac{c_p}{2Nc_t}\alpha^2\omega k_\delta$, $v_n^* = 0$, and $v_\theta^* = 0$, i.e. that it moves in a straight line along the global x-axis. A final powerful feature of Theorem 4 is that it applies to snake robots with an arbitrary number of links N. The relationship between the gait parameters and the average forward velocity of the snake robot can be summarized as follows:

Corollary 1. *Consider a planar snake robot with N links modelled by (73) and controlled in exact accordance with (80) and (81). The average forward velocity of the snake robot will converge exponentially to a value which is proportional to:*

- *the squared amplitude of the sinusoidal joint motion, α^2,*
- *the angular frequency of the sinusoidal joint motion, ω,*
- *the function of the constant phase shift, δ, between the joints given by*

$$k_\delta = \sum_{i=1}^{N-1}\sum_{j=1}^{N-1} a_{ij}\sin\left((j-i)\,\delta\right), \tag{85}$$

where a_{ij} denotes element ij of the matrix $\mathbf{A}\overline{\mathbf{D}}$.

By using (85), the phase shift δ that maximizes the forward velocity of the snake robot can be found. In Liljebäck et al. (2013) the optimal δ is seen to be a decreasing function of the number of links N. The results in this section are validated by simulations and experiments in (Liljebäck et al., 2013, Chapters 7.7-7.9)

5.1.2. Snake robots moving underwater

In this section, we consider snake robots that move underwater using undulatory locomotion according to the general reference signal (71). In particular, the velocity dynamics of the control-oriented model (77) whose joints follow (71) is analyzed using averaging theory.

It is assumed that the joint offset ϕ_0 is constant so that (81) is satisfied. Following the same approach as in Section 5.1.1, it is shown in Kohl et al. (2015b) that under the assumption that

$$|\phi_0| < \frac{N}{2(N-1)} \frac{\sqrt{c_n c_t}}{c_p}, \tag{86}$$

and V_t and V_n are constant, the average velocity, $\mathbf{v}_{av}$, will converge exponentially to the steady state velocity

$$\mathbf{v}^* = \alpha^2 \omega k_\delta \begin{bmatrix} \frac{N c_n c_p}{2(c_n c_t N^2 - 4(N-1)^2 c_p^2 \phi_0^2)} \\ \frac{c_p^2 \phi_0 (N-1)}{c_n c_t N^2 - 4(N-1)^2 c_p^2 \phi_0^2} \\ \frac{N c_n c_p \lambda_2 \phi_0}{2\lambda_1 (c_n c_t N^2 - 4(N-1)^2 c_p^2 \phi_0^2)} \end{bmatrix} + \begin{bmatrix} V_t \\ V_n \\ 0 \end{bmatrix}. \tag{87}$$

Averaging theory gives that for sufficiently large frequencies ω, the average velocity of the snake robot will approximate the exact velocity $\mathbf{v} = [v_t \; v_n \; v_\theta]^T$ given by (77f), (77g), and (77h). This is summarized in the following theorem (see Kohl et al. (2015b) for further details):

Theorem 5. *Consider a snake robot described by (77). Suppose the joint coordinates $\boldsymbol{\phi}$ are controlled in exact accordance with (71) and (81), and that the joint coordinate offset ϕ_o satisfies (86). Then there exist $k > 0$ and $\omega^* > 0$ such that for all $\omega > \omega^*$,*

$$\|\mathbf{v}(t) - \mathbf{v}_{av}(t)\| \leq \tfrac{k}{\omega} \quad \textit{for all } t \in [0, \infty), \tag{88}$$

Furthermore, the average velocity $\mathbf{v}_{av}(t)$ of the snake robot will converge exponentially fast to the steady state velocity $\mathbf{v}^*$ given by (87).

Note that the presence of ocean currents does not influence the stability properties of the snake robot, but shifts the equilibrium of the velocity dynamics. Moreover, by subtracting the ocean current velocities from both sides of (87) we see that the average relative velocities $v_{t,\text{rel}}$ and $v_{n,\text{rel}}$ (79) converge to the same values as the average velocities of the snake robot moving on land (83).

Theorem 5 thus proves mathematically that the general lateral undulation given by (71) enables a snake robot moving underwater with anisotropic drag forces to achieve

forward propulsion (again under the assumption of small joint angles which can be modeled as translational link displacements). It also makes it possible to analyze a scenario that is particularly interesting for motion planning purposes: steady state motion with zero offset $\phi_0 = 0$, which will be shown to be motion in a straight line.

By inserting $\phi_0 = 0$ into (83) and subtracting the current velocities from both sides, the expression

$$\begin{bmatrix} v^*_{t,\mathrm{rel}} \\ v^*_{n,\mathrm{rel}} \\ v^*_{\theta} \end{bmatrix} = \begin{bmatrix} \alpha^2 \omega k_\delta \frac{c_p}{2c_t N} \\ 0 \\ 0 \end{bmatrix} \tag{89}$$

is obtained. It can easily be seen that the relative velocity normal to the robot's orientation is zero, as is the rotational velocity. This means that the robot moves in a straight line, with its absolute normal velocity equal to the normal current velocity. For the forward velocity, the following property can be derived from (89):

Corollary 2. *Consider an underwater snake robot with N links described by* (77) *and controlled in exact accordance with* (71) *and* (81)*. For* $\omega > \omega^*$ *and sufficiently small* ϕ_0 *for* (86) *to hold, the average relative forward velocity of the robot will converge exponentially to* $v^*_{t,\mathrm{rel}}$*, which is proportional to*

- *the squared amplitude of the joints,* α^2*,*
- *the frequency of the gait,* ω*,*
- *a function of the phase shift* δ*, which is given by*

$$k_\delta = \sum_{i=1}^{N-1} \sum_{j=1}^{N-1} a_{ij} g(i) g(j) \sin((j-i)\delta). \tag{90}$$

This result extends the findings of previous studies: In McIsaac and Ostrowski (2003) it was shown that the averaged forward dynamics of a three- and a five-link eel-like robot are captured by a function proportional to the squared amplitude, frequency, and a sum of sinusoidal functions. It also extends the result from Section 5.1.1 where the special case of lateral undulation, yielding $g(i,N) = 1$, and without disturbances like ocean currents, was investigated. Similarly as pointed out in Section 5.1.1, Corollary 2

provides a powerful tool for motion planning: an increase/decrease of the relative forward velocity can be invoked by using α or ω as a control input. Furthermore, the controller can be optimized by finding the optimal phase shift δ that maximizes k_δ for the given number of links and choice of gait.

Kelasidi et al. (2015a) experimentally validated the empirical properties that were derived for underwater snake robots based on a simulation study in Kelasidi et al. (2015b), and the experimental results are also in agreement with the properties presented here.

5.2. Relationship between the gait parameters, the forward velocity and power consumption

In Kelasidi et al. (2016a) a multi-objective optimization problem was formulated to investigate how to choose gait parameters to maximize the forward velocity and at the same time minimize the power consumption of snake robots. The analysis was performed using particle swarm optimization to obtain optimal gait parameters for the gait patterns lateral undulation and eel-like motion. The analysis was conducted using the model of underwater snake robots presented in Kelasidi et al. (2014c), and although some added mass terms were not included in this model, the results are expected to hold also for the model presented in Section 2.4 since the added mass effects are negligible at low speeds, cf. Remark 6. Furthermore, since the model for snake robots moving on land falls out as a special case when the added mass effects are zero, and the drag forces are replaced by friction forces (cf. Remark 5), the qualitative results are expected to hold also when the snake robots move on land.

The analysis in Kelasidi et al. (2016a) shows that there is a clear trade-off between the forward velocity and the power consumption, as should be expected. In particular, the maximum power is consumed in the cases that achieve maximum velocity. Furthermore, the Pareto front analysis illustrates that the power consumption of the robot can be decreased significantly by a minor reduction in the forward velocity for certain choices of gait parameters. For the particular snake robot considered in the simulations, a 44.75% decrease is achieved in the power consumption while the forward velocity is only reduced by 3.57% for a particular choice of gait parameters for lateral undulation.

A similar reduction is also shown for eel-like motion. The multi-objective analysis and corresponding Pareto fronts, therefore, constitute a useful tool for choosing optimal gait parameters in the control design.

6. Snake robot control

From Section 3 we know that under Assumption 7 an undulatory gait pattern will make the snake robot move forward, and from Section 5 we know how to choose the gait parameters. The next question is then how to design a control law to make the robot not only move forward but follow the desired path.

6.1. Path following control

We consider the path following control objective of making the snake robot converge to a desired straight line path and subsequently progress along this path. Without loss of generality, we align the global x-axis with the desired path, such that the position of the robot along the global y-axis, p_y, corresponds to the shortest distance from the CM of the robot to the desired path (i.e. the cross-track error). Then the orientation of the robot, $\bar{\theta}$, which was defined in (8), is the angle that the robot forms with the desired path. The control objective is thus to regulate p_y and $\bar{\theta}$ so that they oscillate about zero, i.e. so that their trajectories trace out a limit cycle containing $\left(p_y = 0, \bar{\theta} = 0\right)$ in its interior. We do not attempt to regulate p_y and $\bar{\theta}$ to zero since we expect the heading and position of the robot to display oscillating behavior during undulatory locomotion.

From the above discussion, the control problem is to design a feedback control law such that for all $t > t_c \geq 0$, there exists a $\tau \in [t, t+T]$ satisfying

$$p_y(\tau) = 0, \tag{91}$$

$$\bar{\theta}(\tau) = 0, \tag{92}$$

where t_c is some (unknown) finite time duration corresponding to the time it takes the snake robot to converge to the desired straight path, and $T > 0$ is some constant that characterizes the time period of the cyclic gait pattern of the snake robot. In other

words, we require that p_y and $\overline{\theta}$ are zero at least once during each cycle of the locomotion since this means that p_y and $\bar{\theta}$ oscillate about zero. Note that we require $\overline{v}_t(t) > 0$ for all $t > t_c$.

6.1.1. Path following control of snake robots moving on land

For snake robots moving on land, we use the gait pattern lateral undulation which is generated by requiring each link angle, ϕ_i, $i \in \{1, \ldots, N-1\}$, to follow the reference signal

$$\phi_{i,\mathrm{ref}}(t) = \alpha \sin(\omega t + (i-1)\delta) + \phi_0. \tag{93}$$

With this gait pattern, the period of the cyclic locomotion considered in control objectives (91) and (92) will be $T = 2\pi/\omega$.

Line-of-sight (LOS) guidance control

In order to steer the snake robot towards the desired straight path (i.e. the global x-axis), we define the heading reference angle according to the line-of-sight (LOS) guidance law

$$\bar{\theta}_{\mathrm{ref}} = -\arctan\left(\frac{p_y}{\Delta}\right), \tag{94}$$

where p_y is the cross-track error, and $\Delta > 0$ is a design parameter referred to as the *look-ahead distance* that influences the rate of convergence to the desired path. This LOS guidance law is commonly used during e.g. path following control of marine surface vessels (see e.g. Fossen, 2011; Fredriksen and Pettersen, 2006). As illustrated in Fig. 13, the LOS angle $\overline{\theta}_{\mathrm{ref}}$ corresponds to the orientation of the snake robot when it is headed towards the point located a distance Δ ahead of itself along the desired path. The value of Δ is important since it determines the rate of convergence to the desired path. In particular, the value of the parameter Δ will influence the transient motion of the robot, giving a well-damped transient motion for large values of Δ and large overshoots or even instability for too small values. When LOS guidance is used for marine vehicles, a rule of thumb is to choose Δ larger than twice the length of the vehicle (see e.g. Fossen (2011)).

The joint offset angle ϕ_o can be used to control the direction of the locomotion, and

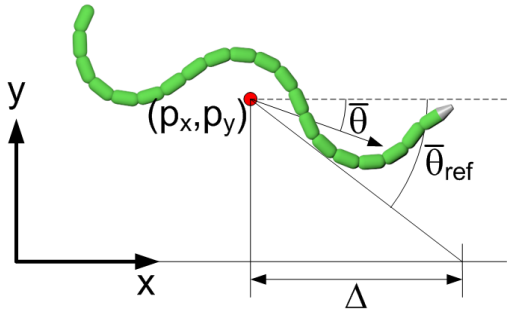

Figure 13: The LOS guidance law.

we, therefore, conjecture that we can control the heading $\bar{\theta}$ to follow the LOS angle given by (94), by defining this joint offset angle as

$$\phi_o = k_\theta \left(\bar{\theta} - \bar{\theta}_{\text{ref}} \right), \tag{95}$$

where $k_\theta > 0$ is a controller gain. To make the joints track the resulting reference angles given by (93), we use the feedback linearizing controller from (Liljebäck et al., 2013, Chapter 2.8), briefly described in Section 2.3, and we let the control input $\overline{\mathbf{u}} \in \mathbb{R}^{N-1}$ be given as

$$\overline{u}_i = k_p \left(\phi_{i,\text{ref}} - \phi_i \right) - k_d \dot{\phi}_i \qquad i = 1, \ldots, N-1, \tag{96}$$

where $k_p > 0$ and $k_d > 0$ are controller gains.

In (Liljebäck et al., 2013, Chapter 5) a Poincaré map analysis is performed which shows that the control objectives (91)–(92) are satisfied for snake robots described by the model (31) with the control law given by (93)–(96). Note, however, that since the Poincaré map analysis is based on simulations, it holds only for the given choice of numerical parameters used in the simulations. To obtain a stability analysis that holds for a general snake robot, we utilize the control-oriented model described in Section 4.2:

LOS guidance control based on the control-oriented model

From the analysis in Section 3 we know that lateral undulation will create propulsive forces, and Corollary 1 gives that the resulting forward velocity is contained in some

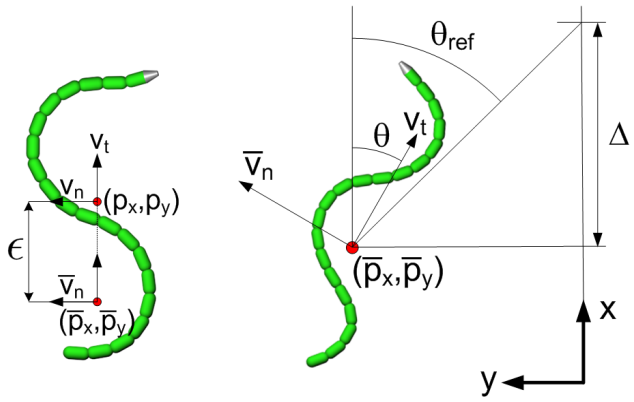

Figure 14: Left: The coordinate transformation of the snake robot. Right: The LOS guidance law (108).

non-zero and positive interval $[V_{\min}, V_{\max}]$ that can be scaled based on the gait pattern parameters. We can thus make the following assumption in the control design:

Assumption 10. *The snake robot moving by lateral undulation has a forward velocity which is always non-zero and positive, i.e.* $v_t \in [V_{\min}, V_{\max}]\ \forall\, t \geq 0$ *where* $V_{\max} \geq V_{\min} > 0$.

By Assumption 10, we can consider the forward velocity v_t as a positive parameter satisfying $v_t \in [V_{\min}, V_{\max}]$.

As seen in (73f) and (73h), the joint coordinates $\boldsymbol{\phi}$ are present in the dynamics of both the angular velocity v_θ and the sideways velocity v_n of the snake robot. This complicates the controller design since the body shape changes will affect both the heading and the sideways motion of the robot. Motivated by Do and Pan (2003) and Fredriksen and Pettersen (2006), we see that it is possible to remove the effect of $\boldsymbol{\phi}$ on the sideways velocity by performing a coordinate transformation. In particular, we move the origin of the body-fixed coordinate system a distance ε from the CM along the tangential direction of the robot, to a new location, denoted the *pivot point*. The pivot point is where the body shape changes of the robot (characterized by $\bar{\mathbf{e}}^T\boldsymbol{\phi}$) generate a pure rotational motion and no sideways force. This coordinate transformation is

illustrated to the left in Fig. 14 and is defined as

$$\overline{p}_x = p_x + \varepsilon \cos\theta, \tag{97a}$$

$$\overline{p}_y = p_y + \varepsilon \sin\theta, \tag{97b}$$

$$\overline{v}_n = v_n + \varepsilon v_\theta, \tag{97c}$$

where ε is a constant parameter defined as

$$\varepsilon = -\frac{2(N-1)}{Nm}\frac{c_p}{\lambda_2}. \tag{98}$$

With the new coordinates given by (97), the model (73) is transformed into

$$\dot{\boldsymbol{\phi}} = \mathbf{v}_\phi, \tag{99a}$$

$$\dot{\theta} = v_\theta, \tag{99b}$$

$$\dot{\overline{p}}_y = v_t \sin\theta + \overline{v}_n \cos\theta, \tag{99c}$$

$$\dot{\mathbf{v}}_\phi = -\frac{c_n}{m}\mathbf{v}_\phi + \frac{c_p}{m} v_t \mathbf{A}\mathbf{D}^T \boldsymbol{\phi} + \frac{1}{m}\mathbf{D}\mathbf{D}^T \mathbf{u}, \tag{99d}$$

$$\dot{v}_\theta = -\lambda_1 v_\theta + \frac{\lambda_2}{N-1} v_t \overline{\mathbf{e}}^T \boldsymbol{\phi}, \tag{99e}$$

$$\dot{\overline{v}}_n = X v_\theta + Y \overline{v}_n, \tag{99f}$$

where, by Assumption 10, the parameter $v_t \in [V_{\min}, V_{\max}]$ with $V_{\max} \geq V_{\min} > 0$, and where

$$X = \varepsilon\left(\frac{c_n}{m} - \lambda_1\right), \tag{100a}$$

$$Y = -\frac{c_n}{m}. \tag{100b}$$

The two scalar constants X and Y have been introduced in (99f) for simplicity of notation. Note also that (73c) is not included in (99) since we do not consider the time evoluation of the position of the system along the path during path following.

The path following control problem for snake robots described by the control-

oriented model (99), is to design a feedback control law

$$\mathbf{u} = \mathbf{u}(t, \boldsymbol{\phi}, \theta, p_y, \mathbf{v}_\phi, v_\theta, v_t, v_n) \in \mathbb{R}^{N-1}, \tag{101}$$

such that the following control objectives are reached:

$$\lim_{t\to\infty} \overline{p}_y(t) = 0, \tag{102}$$

$$\lim_{t\to\infty} \theta(t) = 0. \tag{103}$$

680 **Remark 11.** *The path following control objectives that were given in* (91)-(92) *did not attempt to suppress the oscillatory behavior of the heading and position of the snake robot during undulatory motion along the desired path. However, since the path following controller proposed in the following is based on the control-oriented model of the snake robot, it is possible to prove convergence to zero.*

We use the linearizing control law

$$\mathbf{u} = m\left(\mathbf{D}\mathbf{D}^T\right)^{-1}\left(\overline{\mathbf{u}} + \frac{c_n}{m}\dot{\boldsymbol{\phi}} - \frac{c_p}{m}v_t\mathbf{A}\mathbf{D}^T\boldsymbol{\phi}\right), \tag{104}$$

where $\overline{\mathbf{u}} \in \mathbb{R}^{N-1}$ is a new set of control inputs. This control law transforms the joint dynamics (99d) into $\dot{\mathbf{v}}_\phi = \ddot{\boldsymbol{\phi}} = \overline{\mathbf{u}}$. To make the joints track the joint reference coordinates given by (93), we choose the new control input $\overline{\mathbf{u}}$ to be

$$\overline{\mathbf{u}} = \ddot{\boldsymbol{\phi}}_{\text{ref}} + k_{v_\phi}\left(\dot{\boldsymbol{\phi}}_{\text{ref}} - \dot{\boldsymbol{\phi}}\right) + k_\phi\left(\boldsymbol{\phi}_{\text{ref}} - \boldsymbol{\phi}\right), \tag{105}$$

where $k_\phi > 0$ and $k_{v_\phi} > 0$ are scalar controller gains, and $\boldsymbol{\phi}_{\text{ref}} \in \mathbb{R}^{N-1}$ are the joint reference coordinates given by (93). By introducing the error variable

$$\widetilde{\boldsymbol{\phi}} = \boldsymbol{\phi} - \boldsymbol{\phi}_{\text{ref}}, \tag{106}$$

the joint dynamics given by (99a) and (99d) can be rewritten as the error dynamics

$$\ddot{\widetilde{\boldsymbol{\phi}}} + k_{v_\phi}\dot{\widetilde{\boldsymbol{\phi}}} + k_\phi\widetilde{\boldsymbol{\phi}} = \mathbf{0}, \tag{107}$$

which is clearly *globally exponentially stable*. This implies that the joint coordinates exponentially track the reference signal given by (93).

We use the LOS guidance law, adapted to the coordinates of the transformed control-oriented model (99), cf. Fig. 14:

$$\theta_{\text{ref}} = -\arctan(\frac{\overline{p}_y}{\Delta}), \tag{108}$$

To derive the expression for ϕ_o to control the heading of the robot, we first rewrite the dynamics of v_θ given by (99e) with the new coordinates $\widetilde{\boldsymbol{\phi}}$ in (106), which gives the dynamics of v_θ as a function of the joint reference coordinates given by (93). From (106), we have that $\boldsymbol{\phi} = \boldsymbol{\phi}_{\text{ref}} + \widetilde{\boldsymbol{\phi}}$. By using (93) we can, therefore, rewrite (99e) as

$$\dot{v}_\theta = -\lambda_1 v_\theta + \lambda_2 v_t \phi_o + \frac{\lambda_2}{N-1} v_t \left(\sum_{i=1}^{N-1} \alpha \sin(\omega t + (i-1)\,\delta) + \overline{\mathbf{e}}^T \widetilde{\boldsymbol{\phi}} \right). \tag{109}$$

Consequently, choosing ϕ_o as

$$\phi_o = \frac{1}{\lambda_2 v_t} \left(\ddot{\theta}_{\text{ref}} + \lambda_1 \dot{\theta}_{\text{ref}} - k_\theta(\theta - \theta_{\text{ref}}) - \frac{\lambda_2}{N-1} v_t \sum_{i=1}^{N-1} \alpha \sin(\omega t + (i-1)\,\delta) \right), \tag{110}$$

where $k_\theta > 0$ is a scalar controller gain, enables us to express the dynamics of the heading angle θ, which is given by (99b) and (99e), as the error dynamics

$$\ddot{\widetilde{\theta}} + \lambda_1 \dot{\widetilde{\theta}} + k_\theta \widetilde{\theta} = \frac{\lambda_2}{N-1} v_t \overline{\mathbf{e}}^T \widetilde{\boldsymbol{\phi}}, \tag{111}$$

where we have introduced the error variable

$$\widetilde{\theta} = \theta - \theta_{\text{ref}}. \tag{112}$$

Remark 12. *The joint coordinate offset in (110) depends on the inverse of the forward velocity v_t. This does not represent a problem since, by Assumption 10, the forward velocity is always non-zero. When implementing the path following controller, this issue can be avoided by activating the controller* after *the snake robot has obtained a positive forward velocity through lateral undulation.*

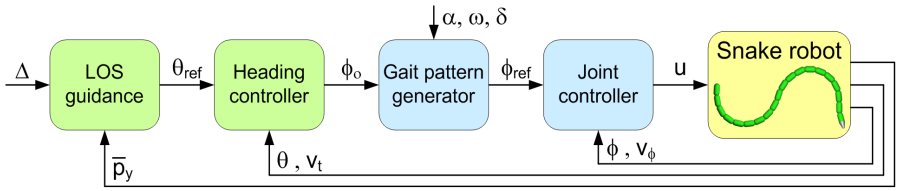

Figure 15: The structure of the LOS-based path following control system.

Remark 13. *The error dynamics of the joints in (107) and the error dynamics of the heading in (111) represent a cascaded system. In particular, the system (107) perturbs the system (111) through the interconnection term* $\frac{\lambda_2}{N-1} v_t \overline{\mathbf{e}}^T \widetilde{\boldsymbol{\phi}}$.

We have now presented the complete path following controller of the snake robot. The structure of the complete control system is summarized in Fig. 15.

By using cascaded systems theory Panteley et al. (1998), Panteley and Loria (2001), it is shown in (Liljebäck et al., 2013, Chapter 8.3.6) that the origin of the closed-loop system is uniformly globally asymptotically stable and locally exponentially stable under a given condition on the control parameter Δ. In particular, the following theorem is proved:

Theorem 6. *Consider a planar snake robot described by the model (99) and suppose that Assumption 10 is satisfied. If the look-ahead distance* Δ *of the LOS guidance law (108) is chosen such that*

$$\Delta > \frac{|X|}{|Y|}\left(1 + \frac{V_{\max}}{V_{\min}}\right), \tag{113}$$

then the path following controller defined by (93), (104), (105), (108), and (110) guarantees that the control objectives (102) and (103) are achieved for any set of initial conditions satisfying $v_t \in [V_{\min}, V_{\max}]$.

Remark 14. *Any gait pattern controller that uniformly globally exponentially stabilizes the error variable (106), i.e. not just the joint controller proposed in (104)-(105), makes the complete cascaded system uniformly globally asymptotically and locally exponentially stable.*

Remark 15. *As explained in Section 4, the assumptions underlying the control-oriented model are only valid as long as the joint angles are small. The stability result in The-*

orem 6 is therefore claimed only for snake robots conducting lateral undulation with limited joint angles.

In (Liljebäck et al., 2013, Chapter 8.4) it is furthermore shown how the straight-line path following controller presented above can be extended to path following also of curved paths.

6.1.2. Path following control of snake robots moving underwater

For snake robots moving underwater, we use the general gait pattern that encompasses both lateral undulation and eel-like motion, and which is generated by requiring each link angle, ϕ_i, $i \in \{1,\ldots,N-1\}$, to follow the reference signal

$$\phi_{i,\text{ref}}(t) = \alpha g(i,N)\sin\left(\omega t + (i-1)\delta\right) + \phi_0. \tag{114}$$

Also with this gait pattern, the period of the cyclic locomotion considered in control objectives (91) and (92) will be $T = 2\pi/\omega$.

Integral line-of-sight (ILOS) guidance control

When the snake robot moves underwater, it will be subject to ocean currents of unknown direction and magnitude, and the path following controller needs to adapt to this. If we were to use a pure LOS guidance law, the ocean current would make the robot drift away from the desired path, giving a stationary cross-track error. To steer the snake robot towards the desired straight path (i.e. the global x-axis), we thus define the heading reference angle by the integral LOS guidance law

$$\bar{\theta}_{\text{ref}} = -\arctan\left(\frac{p_y + \sigma y_{int}}{\Delta}\right), \qquad \Delta > 0, \tag{115}$$

$$\dot{y}_{int} = \frac{\Delta p_y}{(p_y + \sigma y_{int})^2 + \Delta^2}, \tag{116}$$

where p_y is the cross-track error, while both the look-ahead distance Δ and the integral gain $\sigma > 0$ are constant design parameters, and y_{int} represents the integral action of the guidance law. Note that the integral LOS guidance law (115)-(116) includes an

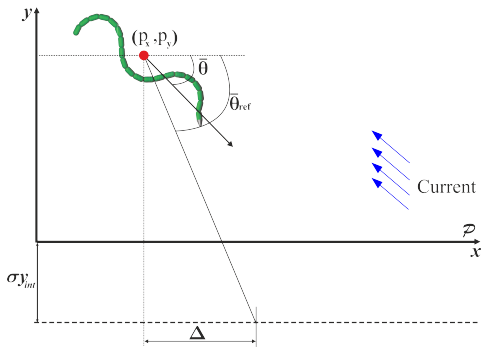

Figure 16: The integral line-of-sight guidance law.

anti-windup effect, as $\dot{y}_{\text{int}}$ converges to zero when the cross-track error p_y is large. The integral LOS path following controller was proposed for straight path following control of marine surface vessels in the presence of unknown constant irrotational ocean current Borhaug et al. (2008), Caharija et al. (2013). Fig. 16 illustrates the intuition behind the integral LOS approach: Instead of heading towards a point that lies a distance Δ ahead of the robot along the global x-axis, as for the original LOS approach, the robot is made to head towards a point that lies a distance Δ ahead of the robot along a displaced axis. The displaced axis lies upstream of the path, and the magnitude of the displacement is proportional to the integrated cross-track error. The intention is to make the robot move along the desired path with the crab angle that is necessary to compensate for the unknown ocean current. In Kelasidi et al. (2017a) a Poincaré map analysis is performed which shows that path following is achieved, and this is also validated by experiments. Again these results only hold for the particular numerical simulation model used in the simulations, and also for the particular physical snake robot employed in the experiments. To prove that an integral-LOS controller achieves path following for a general snake robot, we will also here use the control-oriented model:

Integral LOS guidance control based on the control-oriented model

We consider the control-oriented model (77) for snake robots moving underwater. The development of the model-based integral LOS guidance controller is based on the fol-

lowing assumptions:

Assumption 11. *The ocean current, $v_c = [V_x,\ V_y]^T$, is constant and irrotational in the global frame. It is furthermore bounded by $V_{c,\max} \geq \sqrt{V_x^2 + V_y^2}$.*

Remark 16. *The ocean current will be slowly varying compared to the dynamics of the snake robot, and barring turbulent flow, Assumption 11 is thus a valid assumption.*

Assumption 12. *The underwater snake robot is moving with some constant relative forward velocity $v_{t,\text{rel}} \in [V_{\min}, V_{\max}]\ \forall\ t \geq 0$, where $V_{\max} \geq V_{\min} > 0$.*

Assumption 13. *The forward velocity is large enough to compensate for the current, i.e. $v_{t,\text{rel}} > V_{\min} > V_{c,\max}$.*

Remark 17. *As seen in Corollary 2, when using the general gait pattern* (114) *the relative forward velocity converges to a constant value that can be tuned by the choice of gait parameters α, ω and δ, something which makes Assumption 12 a valid assumption. If the robot actuators are not sufficiently strong to achieve a forward velocity that satisfies Assumption 13, the robot can not achieve path following when subjected to ocean currents of this magnitude.*

From the dynamical equations (77f) and (77h) we see that the joint coordinates ϕ enter the dynamics of both v_θ and v_n. As pointed out in Section 6.1.1, this complicates the design of the control system. We, therefore, apply the same coordinate transformation (97)-(98) as for snake robots moving on land. Furthermore, the absolute velocities are removed from (77) by inserting the relations $[v_t,\ \bar{v}_n]^T = [v_{t,\text{rel}} + V_t,\ \bar{v}_{n,\text{rel}} + V_n]^T$, where $V_t = V_x \cos\theta + V_y \sin\theta$, and $V_n = -V_x \sin\theta + V_y \cos\theta$ are the ocean current velocities expressed in the body frame, and $\dot{\bar{v}}_n = \dot{\bar{v}}_{n,\text{rel}} + \dot{V}_n$, with $\dot{V}_n = -V_t \dot{\theta}$ Fossen (2011).

By using the transformation (97) and the relative velocities, the model can be

rewritten in the new coordinates as

$$\dot{\boldsymbol{\phi}} = \mathbf{v}_\phi, \tag{117a}$$

$$\dot{\theta} = v_\theta, \tag{117b}$$

$$\dot{\bar{p}}_y = v_{t,\mathrm{rel}} \sin\theta + \bar{v}_{n,\mathrm{rel}} \cos\theta + V_y, \tag{117c}$$

$$\dot{\mathbf{v}}_\phi = \bar{\mathbf{u}}, \tag{117d}$$

$$\dot{v}_\theta = -\lambda_1 v_\theta + \tfrac{\lambda_2}{N-1} v_{t,\mathrm{rel}} \bar{\mathbf{e}}^T \boldsymbol{\phi}, \tag{117e}$$

$$\dot{\bar{v}}_{n,\mathrm{rel}} = (X + V_t) v_\theta + Y \bar{v}_{n,\mathrm{rel}}, \tag{117f}$$

where X and Y also here are defined as $X = \varepsilon(\frac{c_n}{m} - \lambda_1), Y = -\frac{c_n}{m}$. By Assumption 12 the relative forward velocity $v_{t,\mathrm{rel}}$ is treated as a positive time-varying parameter. Furthermore, (77c) is not included in (117) since the time evolution of the position along the path is not considered during path following. Furthermore, the linearizing feedback control law

$$\mathbf{u} = m \left(\mathbf{D}\mathbf{D}^T\right)^{-1} \left(\bar{\mathbf{u}} + \frac{c_n}{m} \dot{\boldsymbol{\phi}} - \frac{c_p}{m} v_{t,\mathrm{rel}} \mathbf{A}\mathbf{D}^T \boldsymbol{\phi}\right), \tag{118}$$

has been applied, Kohl et al. (2015b).

Based on the above discussion and model, the path following control objectives can be stated as follows:

$$\lim_{t\to\infty} \bar{p}_y(t) = 0, \tag{119}$$

$$\lim_{t\to\infty} \theta(t) = \theta^{\mathrm{eq}}. \tag{120}$$

The desired heading angle θ^{eq} is constant and $\theta^{\mathrm{eq}} \in (-\frac{\pi}{2}, \frac{\pi}{2})$. The equilibrium heading θ^{eq} will be non-zero for non-zero ocean currents, thus providing the necessary crab angle to compensate for the path transversal current-component, cf. Fig. 16. The magnitude of the required crab angle θ^{eq} will be determined by the magnitude of the ocean current, through the integral effect.

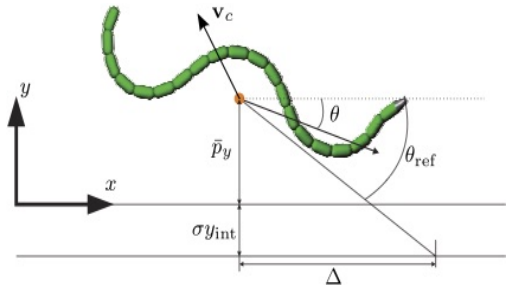

Figure 17: The integral LOS guidance law (123).

Similarly as for snake robots moving on land, we choose the control input $\overline{\mathbf{u}}$ to be

$$\overline{\mathbf{u}} = \ddot{\boldsymbol{\phi}}_{\text{ref}} + k_{v_\phi}\left(\dot{\boldsymbol{\phi}}_{\text{ref}} - \dot{\boldsymbol{\phi}}\right) + k_\phi\left(\boldsymbol{\phi}_{\text{ref}} - \boldsymbol{\phi}\right), \tag{121}$$

where $k_\phi > 0$ and $k_{v_\phi} > 0$ are scalar controller gains, while $\boldsymbol{\phi}_{\text{ref}} \in \mathbb{R}^{N-1}$ for underwater robots are the joint reference coordinates given by (114). The resulting joint dynamics given by (117a) and (117d) can be expressed by the dynamics of the error variable $\widetilde{\boldsymbol{\phi}} = \boldsymbol{\phi} - \boldsymbol{\phi}_{\text{ref}}$:

$$\ddot{\widetilde{\boldsymbol{\phi}}} + k_{v_\phi}\dot{\widetilde{\boldsymbol{\phi}}} + k_\phi\widetilde{\boldsymbol{\phi}} = \mathbf{0}, \tag{122}$$

which is clearly *globally exponentially stable*, such that the joint coordinates exponentially track the reference signal given by (114).

We use the integral LOS guidance law, adapted to the coordinates of the transformed control-oriented model (117), cf. Fig. 17:

$$\theta_{\text{ref}} = -\arctan\left(\frac{\bar{p}_y + \sigma y_{\text{int}}}{\Delta}\right), \tag{123a}$$

$$\dot{y}_{\text{int}} = \frac{\Delta \bar{p}_y}{(\bar{p}_y + \sigma y_{\text{int}})^2 + \Delta^2}, \tag{123b}$$

By similar arguments as for snake robots on land, we choose the joint offset as

$$\phi_o = \frac{1}{\lambda_2 v_{t,\text{rel}}}\left(\ddot{\theta}_{\text{ref}} + \lambda_1\dot{\theta}_{\text{ref}} - k_\theta(\theta - \theta_{\text{ref}}) - \frac{\lambda_2}{N-1}v_{t,\text{rel}}\sum_{i=1}^{N-1}\alpha g(i,N)\sin(\omega t + (i-1)\,\delta)\right). \tag{124}$$

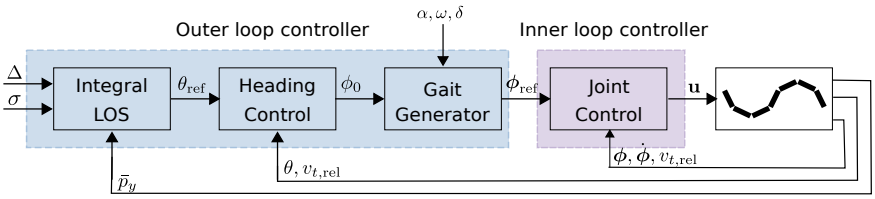

Figure 18: The structure of the integral LOS-based path following control system

which yields the following error dynamics of the heading angle:

$$\ddot{\tilde{\theta}} + \lambda_1 \dot{\tilde{\theta}} + k_\theta \tilde{\theta} = \tfrac{\lambda_2}{N-1} v_{t,\text{rel}} \bar{\mathbf{e}}^T \tilde{\boldsymbol{\phi}}. \tag{125}$$

775 **Remark 18.** *In* (124)*, a singularity will occur when* $v_{t,\text{rel}} = 0$*. When implementing the control system, the singularity problem can also here be circumvented by starting the heading controller after the snake robot has gained a sufficiently large forward velocity through undulations.*

The structure of the closed-loop system is shown in Fig. 18 and has a cascaded structure
780 that can be analyzed using cascaded systems analysis tools. It can then be shown that the following result holds (Kohl et al. (2016b)):

Theorem 7. *Consider a fully submerged, neutrally buoyant snake robot described by* (117) *that moves in a plane according to* (114)*, and is exposed to ocean currents. Suppose that Assumptions 11 to 13 are fulfilled. If the look-ahead distance* Δ *and the integral gain* σ *of the ILOS guidance law* (123) *are chosen such that*

$$\Delta > \frac{|X| + 2V_{c,\max}}{|Y|} \left[\frac{5}{4} \frac{V_{\max} + V_{c,\max} + \sigma}{V_{\min} - V_{c,\max} - \sigma} + 1 \right], \tag{126a}$$

$$0 < \sigma < V_{\min} - V_{c,\max}, \tag{126b}$$

then the path following controller defined by (114), (118) *(121), (123), and (124) guarantees that the control objectives* (119) *and* (120) *are achieved for any set of initial*

conditions satisfying $v_{t,\mathrm{rel}} \in [V_{\min}, V_{\max}]$. *Control objective* (120) *is met with*

$$\theta^{\mathrm{eq}} = -\arctan\left(\frac{V_y}{\sqrt{v_{t,\mathrm{rel}}^2 - V_y^2}}\right). \tag{127}$$

Remark 19. *The analysis in Kohl et al. (2016b) shows that any gait pattern controller that uniformly globally exponentially stabilizes the error variable* $\widetilde{\boldsymbol{\phi}}$*, i.e. not just the joint controller proposed in (118),(121), makes the complete cascaded system uniformly globally asymptotically and locally exponentially stable.*

Remark 20. *As explained in Section 4, the assumptions underlying the control-oriented model are only valid as long as the joint angles are small. The stability result in Theorem 7 is therefore claimed only for snake robots conducting undulatory locomotion with limited joint angles.*

Theorem 7 is experimentally validated in Kohl et al. (2017).

While the LOS path following control for straight paths can be extended to path following of curved paths for snake robots moving on land, it is not straightforward to extend the ILOS path following control to curved paths for snake robots moving underwater. In particular, when the desired path is curved, the path transverse component of the ocean current changes as the robot moves along the path, and the integral action does not handle this time-varying disturbance as well as it handles constant disturbances.

6.2. Maneuvering control

For some applications, it is desirable also to control the forward velocity of the robot. Instead of using tuning of the gait pattern parameters based on Section 5, we then include feedback control of the forward velocity in the control law. Controlling the forward velocity in addition to path following is denoted *maneuvering* (Skjetne et al. (2004)).

In Mohammadi et al. (2015) and Kohl et al. (2016a), a control strategy is proposed for maneuvering control of land-based and underwater snake robots. The proposed

feedback control strategy enforces virtual constraints to produce undulatory locomotion. The biologically inspired virtual holonomic constraints (VHCs) come from adapting the reference signal for the single joints 71 in the following way:

$$\phi_{i,\mathrm{ref}}(\lambda,\phi_0) = \alpha g(i)\sin\Big(\lambda + (i-1)\delta\Big) + \phi_0, \tag{128}$$

where λ and ϕ_0 are the states of the two dynamic compensators

$$\ddot{\lambda} = u_\lambda, \quad \ddot{\phi}_0 = u_{\phi_0}, \tag{129}$$

with the new control inputs u_λ, u_{ϕ_0}. Note that in (128) the time signal t no longer appears explicitly. Instead, the dynamic gait time evolution is governed by the state of the compensators in (129) and the new inputs u_λ and u_{ϕ_0}.

The proposed VHCs are then the state-dependent relations $\phi_i = \phi_{i,\mathrm{ref}}(\lambda,\phi_0), i \in \{1,\dots,N-1\}$. The state ϕ_0 is used to control the orientation, while the state λ is used to control the forward velocity (relative forward velocity resp.) of the snake robot. Note that $\dot{\lambda}$ is the frequency of the sine function in (128), and we hence use the frequency of the undulations to control the forward velocity of the robot. This is in line with Corollaries 1-2 which show a linear dependence between the frequency and the average forward velocity (relative forward velocity, resp.), making the frequency an efficient choice as a virtual control input for velocity control.

VHCs make the control design amenable to a hierarchical synthesis (Seibert and Florio (1995); El-Hawwary and Maggiore (2013)), where the biological gaits are enforced at the lowest level of hierarchy and path planning is done for a point-mass abstraction of the snake robot at the highest level of hierarchy Mohammadi et al. (2014, 2015):

- ***Stage 1*** *Body shape controller that enforces the VHCs*

  This stage represents the inner control loop and has the highest priority. The control torque $\mathbf{u}$ of the snake robot ((28a), alt. (54)) is used to stabilize the VHCs (128). The controller is an input-output feedback linearizing controller that directly imposes the VHCs by stabilizing $e_i = \phi_i - \phi_{i,\mathrm{ref}}(\lambda,\phi_0),\ \ i \in \{1,\dots,N-1\}$.

Once the VHCs are enforced, the system dynamics evolve according to (128), and the states λ and ϕ_0 can be interpreted as new inputs for the second stage of the control design.

- ***Stage 2*** *Velocity controller that consists of a heading and a speed controller*

  At this stage, the inputs u_{ϕ_0} and u_λ of the two dynamic compensators (129) are designed. First, u_{ϕ_0} is designed such that the head angle, θ_N, of the snake robot is practically stabilized to a reference heading $\theta_{\text{ref}}(\mathbf{p})$. Secondly, u_λ is designed such that the forward velocity v_t ($v_{t,\text{rel}}$ resp.) is practically stabilized to the reference speed $v_{\text{ref}}(\mathbf{p})$ ($v_{t,\text{rel}_{\text{ref}}}(\mathbf{p})$ resp.). The references $\theta_{\text{ref}}(\mathbf{p})$ and $v_{\text{ref}}(\mathbf{p})$ ($v_{t,\text{rel}_{\text{ref}}}(\mathbf{p})$ resp.) are derived from the reference velocity vector $\boldsymbol{\mu}$ that is assigned by the third control stage.

- ***Stage 3*** *Path-following controller that provides the reference signals for the velocity controller*

  This is the final stage of the control design with the lowest priority. At the last stage of the control hierarchy, the reference signals for Stage 2, $\theta_{\text{ref}}(\mathbf{p})$ and $v_{\text{ref}}(\mathbf{p})$ ($v_{t,\text{rel}_{\text{ref}}}(\mathbf{p})$ resp.) are designed to make the robot approach the path and follow it with the desired speed. For underwater applications, where the snake robot is exposed to ocean currents, the third stage of the control hierarchy includes the design of an ocean current observer to compensate for the perturbing effect of ocean currents.

Please see Mohammadi et al. (2015) and Kohl et al. (2016a) for the equations describing the control law and the ocean current observer that is derived through this approach. (See Fig. 19 for an illustration of the control approach for underwater snake robots.) By using a reduction theorem for the stability of nested closed sets, practical stability (Teel and Praly (1995)) is shown for the resulting closed-loop system, thus achieving both the path following and velocity control objectives, i.e. solving the maneuvering control problem.

Remark 21. *The control laws are derived based on the models in Section 2 (with the assumptions of negligible added mass (Remark 6) and constant irrotational ocean cur-*

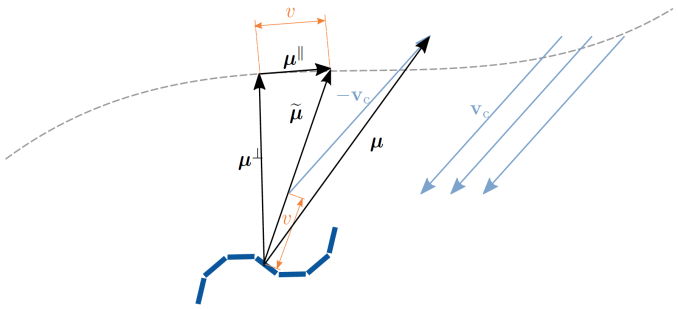

Figure 19: The maneuvering controller with current compensation.

rent, for the underwater snake robots). The results, therefore, do not rely on the simplifying assumption of small link angles like the controllers derived in the previous sections, which were based on the control-oriented models from Section 4, cf. Remarks 15 and 20. Furthermore, an ocean current observer is applied instead of integral action for the control system in the underwater case, something which yields results for general paths, including both curved and straight line paths. Since the models in Section 2 are used, oscillations around the origin are expected, as discussed in Section 6.1 and described in (91)-(92)*, and this is achieved by the practical stability results.*

7. Underwater swimming manipulators (USMs)

The snake robots and results presented in the previous sections are all purely bio-motivated. A natural next question was: "What if we combine the best from biology with the best from technology, and equip the snake robot with additional effectors?" In particular, for the underwater snake robots, a natural next step was to investigate what can be achieved by equipping the robot with thrusters along its body. By combining the slender, multi-articulated and thus flexible body of snakes with the efficient propulsion provided by thrusters, we obtain a new type of robot that is called an underwater swimming manipulator (USM), Sverdrup-Thygeson et al. (2016b), Sverdrup-Thygeson et al. (2017a). This robot may constitute the next generation intervention AUV, which is the next step in the line of ROVs and AUVs for subsea operations (Kelasidi et al. (2016b)). A generic illustration is given in Fig. 20. The thrusters give the robot hov-

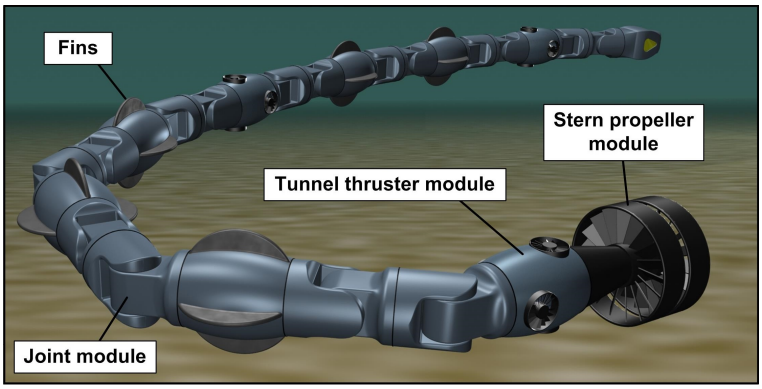

Figure 20: Generic illustration of a USM

ering capabilities in addition to faster propulsion, while the snake-like body provides the robot with beneficial hydrodynamic properties for long-distance transportation, and exceptional access to narrow areas. Also, equipping the robot with sensors and tools, the multi-articulated body constitute a dexterous robot manipulator arm that can perform inspection and intervention operations subsea, operating as a floating base robotic manipulator.

Mathematical models of the USM are derived in Sverdrup-Thygeson et al. (2016b) and Kelasidi et al. (2017b). Since the links of the USM generally will be different, depending on the size and number of the actuators, the length and mass of the links can be different. The model in Section 2.4 falls out as a special case when all the links have the same length and mass, and there are no forces from additional effectors.

Sverdrup-Thygeson et al. (2016a) and Sverdrup-Thygeson et al. (2017a) present a generic motion control framework for the USM, as shown in Fig. 21. The framework itself resembles a typical guidance, control, and thrust allocation system for marine vehicles (Fossen (2011)). However, the challenges faced by the different subsystems are more complex for a USM, due to kinematic redundancy (with the additional effectors, the robot generally becomes overactuated for the task of controlling its position and orientation), multi-body dynamics, dynamic coupling effects, and a state dependent thruster configuration matrix.

Motion planning

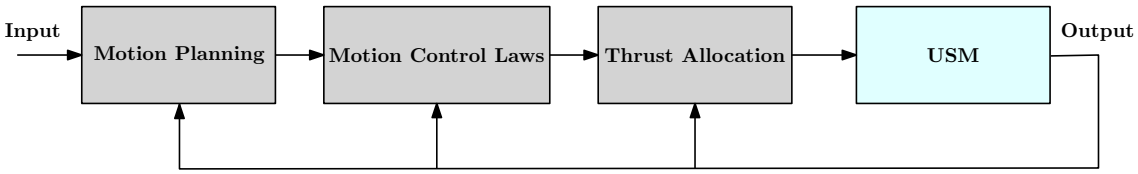

Figure 21: Motion control framework for the USM

The motion planning (guidance), generates the reference signals to the dynamic controllers for the joints and the thrusters. The objective of the motion planning module is therefore to specify the desired motion of the joints and the desired position and orientation of the USM, i.e. controlling the USM in the configuration space. Which algorithm that is best suited for this will typically depend on the given task:

Transport Mode: Moving the USM from its starting point to an area of interest will require the USM to follow a path, either pre-planned or created on-the-fly. One control approach is to use the joint angles for directional control while the propulsion of the robot is provided by the thrusters(Sverdrup-Thygeson et al. (2017a), Sans-Muntadas et al. (2017)). This approach is particularly relevant when the USM only has thruster forces acting in the longitudinal direction, for instance through aft thrusters, and no thruster control force in the sideways direction. The robot then functions as an articulated AUV with improved maneuverability compared to rigid AUVs that use rudders for directional control. The reference heading, $\bar{\theta}_{\text{ref}}$, of the USM is then given by a guidance law, and the joint angle references are chosen as

$$\phi_{i,\text{ref}} = g(i,N)\phi_0, \tag{130}$$

$$\phi_0 = k_p(\bar{\theta} - \bar{\theta}_{\text{ref}}) + k_i \int_{t_0}^{t} (\bar{\theta}(\tau) - \bar{\theta}_{\text{ref}}(\tau) d\tau) + k_d(\dot{\bar{\theta}} - \dot{\bar{\theta}}_{\text{ref}}), \tag{131}$$

where k_p, k_d and k_i are control gain parameters, and $g(i,N)$ is a function that distributes the joint action along the body of the robot. For instance, one may want to keep the head quite still to stabilize a head-mounted camera stream, and mainly use the tail part for directional control, and then $g(i,N)$ is chosen to decrease from tail to head. The reference heading $\bar{\theta}_{\text{ref}}$ can, for instance, be given by the integral LOS guidance law (123). By using a standard PID control law to generate the required thruster forces to achieve

the desired forward speed, and tuning the control parameters properly, a smooth motion and fast convergence to the desired path can be achieved, while keeping the required thruster forces and joint angles within the actuator limitations. For further details, the reader is referred to Sverdrup-Thygeson et al. (2016b), where also simulation results are presented that validate the LOS guidance control for USMs. Furthermore, in Sans-Muntadas et al. (2017) experiments are presented that validate this approach for path following of spiral paths, achieving autonomous docking of USMs.

Work mode: When the USM has reached the target position and is set to perform an inspection or intervention operation, a typical task would then be to control the motion of the USM end-effector, i.e. the head link of the USM. The desired end-effector motion will typically be specified by a human operator or by a high-level autonomy system. Moving the end-effector of the USM can be made either by moving the whole USM as a rigid body using the thrusters or by changing the joint angles. Together this constitutes a system with a high degree of kinematic redundancy, and thus, there are infinitely many ways to fulfill the end-effector positioning task. To this end, it is useful to utilize the inherent redundancy of the USM to achieve the satisfaction of multiple objectives simultaneously. While the primary objective is given by the desired end-effector motion, the USM allows for several alternative secondary control objectives. The secondary control objectives for USMs may typically be:

1. Satisfy the mechanical constraints, e.g. the maximum joint deflections and maximum angular velocity for the joints
2. Maintain good manipulability, i.e. avoid singular joint configurations
3. Maintain controllability, i.e. avoid singular thruster configurations
4. Avoid collision with other moving objects and stationary obstacles
5. Minimize the total thruster effort
6. Minimize drag forces, i.e. attempt to align the USM with the dominant direction of the ocean currents

In Sverdrup-Thygeson et al. (2017b) it is shown how kinematic singularity avoidance can be guaranteed using set-based singularity avoidance tasks within the singularity-robust multiple task priority framework. In particular, the USM achieves a desired

position and orientation of the end-effector, and a desired position of the USM base, at the same time as high manipulability is accomplished through kinematic singularity avoidance.

Motion control laws

The motion control laws calculate the prescribed joint torques and generalized thruster forces and moments on the USM, based on the reference signals from the motion planning module. The latter may, for instance, be given by a simple proportional control law for the velocity of the USM base:

$$\tau_c = k\left(V_{0b,d}^b - V_{0b}^b\right), \tag{132}$$

where τ_c is the vector of generalized thruster forces and moments, k is the proportional gain factor, and

$$V_{0b}^b = \begin{bmatrix} v_{0b}^b \\ \omega_{0b}^b \end{bmatrix} \in \mathbb{R}^6, \tag{133}$$

where v_{0b}^b and ω_{0b}^b are the body-fixed linear and angular velocities of the base of the USM, respectively. In Sverdrup-Thygeson et al. (2017a) this control law is applied in 3D simulations in an underwater environment, where it is combined with both kinematic and dynamic control.

Thrust allocation

Thrust allocation is the process of distributing the commanded generalized forces and moments between the thrusters. For a typical underwater vehicle, each thruster has a fixed position and orientation relative to the body-fixed reference frame. The thrusters are usually mounted in pairs and aligned with the axes of rotation, such that they affect only the axes that need to be controlled. However, this is not the case for the USM. When the shape of the USM changes, the position and orientation of the thrusters with respect to the base of the USM also change. The thrust allocation algorithm must therefore take into account that the thruster configuration matrix is a function of the

joint angles. In addition, the complex multi-body dynamics of the USM indicates that the USM should be fully actuated at all times, in order to control the overall motion of the USM base in 6 DOF. Mathematically, this means that the thruster configuration matrix must have row rank equal to six for all attainable joint configurations. If the USM should exhibit an underactuated thruster configuration, the USM may experience undesirable rotational motion.

If the USM has more thrusters than required to satisfy the given control task, it is referred to as an overactuated system. In this case, the solution to the thrust allocation problem is not unique, i.e. there are infinitely many ways to distribute the thrust forces and yet obtain the same generalized forces and moments. In Sverdrup-Thygeson et al. (2016a) and Sverdrup-Thygeson et al. (2017a) thrust allocation algorithms are discussed, and the following alternatives are proposed as optimization criteria:

- Minimize some measure of the combined thruster efforts.
- Minimize the single largest thrust force.
- Minimize the thrust force fluctuations, i.e. the time-derivative of the thrust forces.

8. Subsea inspection and intervention - towards industrial use

The beneficial properties of the USM make it an interesting robot for subsea operations. For several decades, the traditional remotely operated vehicle (ROV) has been the workhorse used for any kind of subsea operation. Currently, the industry is facing an important shift towards more economical and more efficient operations on subsea installations, and the use of conventional ROVs deployed from surface support vessels is, in many situations, considered too expensive. The number of subsea installations for oil and gas production are increasing. Existing subsea infrastructure is aging, requiring more preventive maintenance, at the same time as the needs for routine inspections increase as the number of new subsea installations continue to grow. Consequently, the industry has recognized the need for smaller, less costly, and more specialized vehicles that can perform various autonomous and semi-autonomous tasks at subsea oil

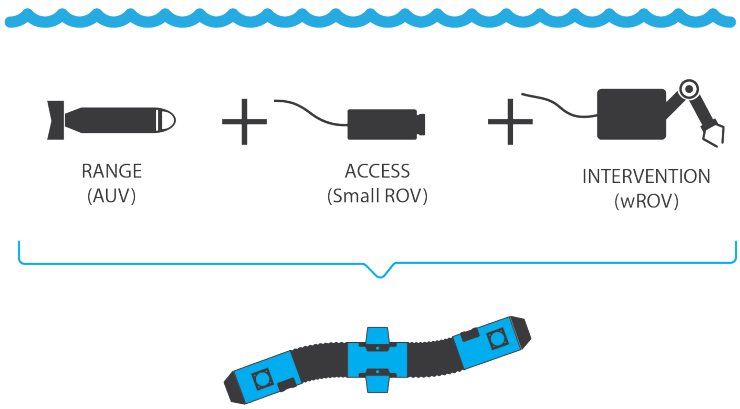

Figure 22: The features of the USM. Courtesy of Eelume.

and gas installations (Gilmour et al. (2012)). In particular, small, lightweight AUVs with hovering and precise maneuvering capabilities gain increased attention.

The USM combines several beneficial features of survey AUVs, work class ROVs and observation ROVs and AUVs into one tool, cf. Fig. 22; It shares the same advantageous hydrodynamic properties as the survey AUV, making it suitable for long range transportation. The flexible and slender body can access and operate in restricted areas of subsea structures, achieving excellent access capabilities compared to small observation ROVs/AUVs. Furthermore, the vehicle itself is a dexterous robotic arm which can operate tools and carry out intervention tasks, operating as a floating base robotic manipulator.

The combined features of the USM make it an excellent choice for a subsea resident robot, which will be permanently installed on the seabed, being ready 24/7 for planned and on-demand inspection and intervention operations. This solution will dramatically save costs by reducing the use of expensive surface vessels which are needed to support such operations today. Eelume AS (Eelume (2015)) is a company sourced from the Norwegian University of Science and Technology (NTNU) and has teamed up with Kongsberg Maritime and Statoil to develop this robot for industrial use.

Eelume vehicles can be installed on both existing and new fields where typical jobs include; visual inspection, cleaning, and operating valves and chokes. These jobs account for a large part of the total subsea inspection and intervention spend. The

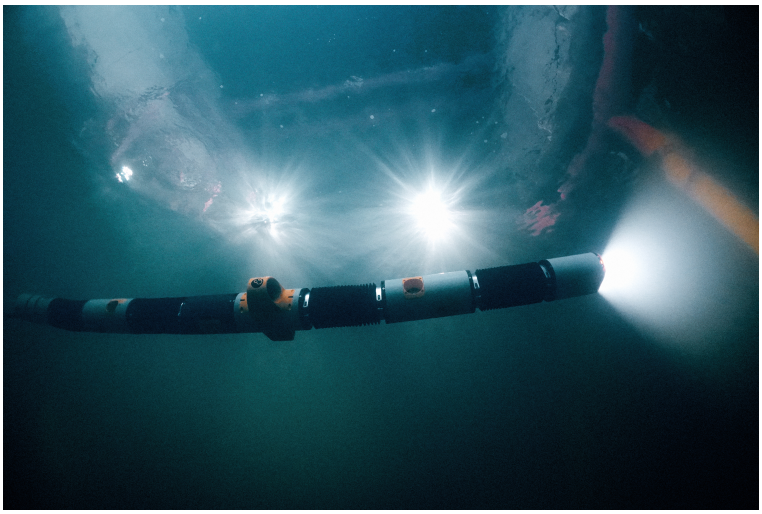

Figure 23: The Eelume robot hovering underwater. Courtesy of Eelume.

first prototype, Fig. 23, was tested in the deep waters of the Trondheim fjord and at the PREZIOSO Linjebygg Subsea Test Center in Trondheim, in December 2016. The purpose of the testing was to verify and demonstrate the features of Eelume's snake-like underwater robot in a deep-water, marine environment. Eelume confirmed that the vehicle has superior maneuverability, is a stable sensor and actuator platform, and has easy access to constrained areas not accessible by conventional underwater vehicles. The next prototype is currently under development and will be tested down to 500 m in 2017, also demonstrating the intervention capabilities. While the robot is developed as a subsea resident robot for the oil and gas industry, it is also a highly applicable tool for subsea operations within marine biology, archaeology, aquaculture, and port security.

9. Conclusions

This paper has reviewed a selection of recent work by the author's research group on modeling, analysis, and control of snake robots. The kinematics and dynamics of snake robots moving in 2D on land and underwater have been presented. Based on these models, it was shown that if the friction or drag force coefficients of snake robots are larger in the sideways direction than in the longitudinal direction of the robot links, the snake robot achieves forward propulsion by continuously changing its body shape

to induce either ground friction forces or hydrodynamic drag forces that propel the robot forward. This is achieved when the snake robot follows an undulatory gait pattern. The nature of undulatory locomotion allowed us to develop simpler mathematical models, which capture the essential behavior of snake robots during undulatory locomotion, and which are well-suited for analysis and control design.

Based on these models, we derived the relationship between the gait parameters and the forward velocity, such that we can choose the gait parameters to achieve the desired forward velocity and also make an informed trade-off between forward velocity and power consumption. We then developed path following controllers for snake robots. For snake robots moving on land, a line-of-sight (LOS) guidance control law was proposed and shown to exponentially stabilize the desired straight line path under a given condition on the look-ahead distance parameter. For snake robots moving underwater, ocean currents of unknown direction and magnitude need to be handled, and an integral line-of-sight (ILOS) guidance control law was proposed and shown to exponentially stabilize the desired straight line path under given conditions on the look-ahead distance and integral gain parameters. For some applications, it is desirable also to control the forward velocity of the robot. Instead of using tuning of the gait pattern parameters based on the relationship between these parameters and the velocity, which constitute open-loop control of the velocity, we then included feedback control of the forward velocity in the control law, solving the maneuvering control problem. Maneuvering control laws, based on biologically inspired virtual holonomic constraints, were proposed for snake robots moving both on land and underwater.

The paper furthermore presented the underwater swimming manipulator (USM), which is essentially a crossover between an autonomous underwater vehicle (AUV) and an underwater snake robot (USR). The USM is a multi-body articulated structure, but unlike conventional USRs, the USM is equipped with additional thrusters, thus enabling it to operate as a floating base robotic manipulator. The USM combines the slender, multi-articulated and thus flexible body of snakes with the efficient propulsion provided by thrusters. The thrusters give the robot hovering capabilities in addition to faster propulsion, while the snake-like body provides the robot with beneficial hydrodynamic properties for long-distance transportation, and exceptional access to narrow

areas. Furthermore, equipping the robot with sensors and tools, the multi-articulated body constitute a dexterous robot manipulator arm that can perform inspection and intervention operations subsea.

The beneficial properties of the USM make it an interesting robot for subsea operations. It shares the same beneficial hydrodynamic properties as the survey AUV, making it suitable for long range transportation. The flexible and slender body can access and operate in restricted areas of subsea structures, achieving excellent access capabilities compared to small observation ROVs/AUVs. Furthermore, the vehicle itself is a dexterous robotic arm which can operate tools and carry out intervention tasks, operating as a floating base robotic manipulator. The combined features of the USM make it an excellent choice for a subsea resident robot, which will be permanently installed on the seabed, being ready 24/7 for planned and on-demand inspection and intervention operations. This solution will dramatically save costs by reducing the use of expensive surface vessels, which are needed to support such operations today. Eelume AS is a company sourced from the Norwegian University of Science and Technology (NTNU) and has teamed up with Kongsberg Maritime and Statoil to develop this robot for industrial use, and the Eelume robot was successfully tested in the Trondheim Fjord December 2016.

10. Acknowledgments

The author thanks Eleni Kelasidi, Jan Tommy Gravdahl, Anna Kohl, Pål Liljebäck and Jørgen Sverdrup-Thygeson for all their inputs to the preparation of this paper.

References

Bauchot, R., 1994. Snakes: A Natural History. Sterling Publishing Company.

Borhaug, E., Pavlov, A., Pettersen, K.Y., 2008. Integral LOS control for path following of underactuated marine surface vessels in the presence of constant ocean currents, in: Proc. 47th IEEE Conference on Decision and Control (CDC), Cancun. pp. 4984–4991.

Boyer, F., Porez, M., Khalil, W., 2006a. Macro-continuous computed torque algorithm for a three-dimensional eel-like robot. IEEE Transactions on Robotics 22, 763 –775.

Boyer, F., Porez, M., Khalil, W., 2006b. Macro-continuous computed torque algorithm for a three-dimensional eel-like robot. IEEE Trans. Robot. 22, 763–775.

Briggs, B., 2017. Sarcos' snake robot could be coming to a small space near you – to save lives. URL: https://blogs.microsoft.com/transform/feature/sarcos-snake-robot-could-be-coming-to-small-space-near-you-to-save-lives. [Online; posted 1-May-2017].

Caharija, W., Pettersen, K.Y., Sorensen, A., Candeloro, M., Gravdahl, J., 2013. Relative velocity control and integral line of sight for path following of autonomous surface vessels: Merging intuition with theory. Part M: Journal of Engineering for the Maritime Environment 228, 180–191.

Chirikjian, G., Burdick, J., 1990. An obstacle avoidance algorithm for hyper-redundant manipulators, in: Proc. IEEE Int. Conf. Robotics and Automation, pp. 625–631.

Chirikjian, G., Burdick, J., 1995. The kinematics of hyper-redundant robot locomotion. IEEE Trans. Robot. Autom. 11, 781–793.

Colgate, J., Lynch, K., 2004. Mechanics and control of swimming: A review. IEEE Journal of Oceanic Engineering 29, 660–673.

Crespi, A., Ijspeert, A.J., 2008. Online optimization of swimming and crawling in an amphibious snake robot. IEEE Transaction on Robotics 24, 75–87.

Crespi, R., Badertscher, A., Guignard, A., Ijspeert, A.J., 2005. Amphibot I: an amphibious snake-like robot. Robotics and Autonomous Systems 50, 163–175.

Do, K., Pan, J., 2003. Global tracking control of underactuated ships with off-diagonal terms, in: IEEE Conf. Decision and Control, pp. 1250–1255.

Eelume, 2015. URL: http://www.eelume.com.

El-Hawwary, M., Maggiore, M., 2013. Reduction theorems for stability of closed sets with application to backstepping control design. Automatica 49, 214–222.

Fan, S., Woolsey, C., 2013. Underwater vehicle control and estimation in nonuniform currents, in: Proc. American Control Conference (ACC), Washington, DC. pp. 1400–1405.

Fossen, T.I., 2011. Handbook of Marine Craft Hydrodynamics and Motion Control. John Wiley & Sons, Ltd.

Fredriksen, E., Pettersen, K.Y., 2006. Global κ-exponential way-point maneuvering of ships: Theory and experiments. Automatica 42, 677 – 687.

Fukushima, H., Satomura, S., Kawai, T., Tanaka, M., Kamegawa, T., Matsuno, F., 2012. Modeling and control of a snake-like robot using the screw-drive mechanism. IEEE Transactions on Robotics 28, 541–554.

Gilmour, B., Niccum, G., O'Donnell, T., 2012. Field resident AUV systems - Chevron's long-term goal for AUV development, in: Proc. IEEE/OES Autonomous Underwater Vehicles (AUV), Southampton, England. pp. 1–5.

Guizzo, E., Ackerman, E., 2017. Boston dynamics officially unveils its wheel-leg robot: "best of both worlds". URL: `http://spectrum.ieee.org/automaton/robotics/humanoids/boston-dynamics-handle-robot`. [Online; posted 27-February-2017].

Hatton, R., Choset, H., 2009. Approximating displacement with the body velocity integral, in: Proc. Robotics: Science and Systems.

Hirose, S., 1993. Biologically Inspired Robots: Snake-Like Locomotors and Manipulators. Oxford University Press.

Hirose, S., Yamada, H., 2009. Snake-like robots [tutorial]. IEEE Robotics Automation Magazine 16, 88–98.

Hopkins, J., Spranklin, B., S.K., G., 2009. A survey of snake-inspired robot designs. Bioinspiration and Biomimetics 4.

Hu, D., Nirody, J., Scott, T., Shelley, M., 2009. The mechanics of slithering locomotion. Proc. National Academy of Sciences 106, 10081–10085.

Kelasidi, E., Jesmani, M., Pettersen, K.Y., Gravdahl, J.T., 2016a. Multi-objective optimization for efficient motion of underwater snake robots. Artificial Life and Robotics 21, 411–422.

Kelasidi, E., Liljebäck, P., Pettersen, K.Y., Gravdahl, J.T., 2015a. Experimental investigation of efficient locomotion of underwater snake robots for lateral undulation and eel-like motion patterns. Robotics and Biomimetics 2, 1–27.

Kelasidi, E., Liljebäck, P., Pettersen, K.Y., Gravdahl, J.T., 2016b. Innovation in underwater robots: Biologically inspired swimming snake robots. IEEE Robotics Automation Magazine 23, 44–62.

Kelasidi, E., Liljebäck, P., Pettersen, K.Y., Gravdahl, J.T., 2017a. Integral line-of-sight guidance for path following control of underwater snake robots: Theory and experiments. IEEE Transactions on Robotics 33, 610–628.

Kelasidi, E., Pettersen, K.Y., 2017. Modeling of underwater snake robots, in: Ang Jr., M.H., Khatib, O., Siciliano, B. (Eds.), Encyclopedia of Robotics. Springer.

Kelasidi, E., Pettersen, K.Y., Gravdahl, J., 2014a. Modeling of underwater snake robots moving in a vertical plane in 3D, in: Proc. IEEE/RSJ International Conference on Intelligent Robots and Systems (IROS), Chicago, Illinois. pp. 266–273.

Kelasidi, E., Pettersen, K.Y., Gravdahl, J.T., 2015b. Energy efficiency of underwater snake robot locomotion, in: Proc. 23th Mediterranean Conference on Control Automation (MED), Torremolinos, Spain.

Kelasidi, E., Pettersen, K.Y., Gravdahl, J.T., Liljebäck, P., 2014b. Modeling of underwater snake robots, in: Proc. IEEE International Conference on Robotics and Automation (ICRA), Hong Kong, China. pp. 4540–4547.

Kelasidi, E., Pettersen, K.Y., Gravdahl, J.T., Strømsøyen, S., Sørensen, A.J., 2017b. Modeling and propulsion methods of underwater snake robots, in: Proc. 1st IEEE Conference on Control Technology and Applications, Kohala Coast, Hawaii.

Kelasidi, E., Pettersen, K.Y., Liljebäck, P., Gravdahl, J.T., 2014c. Integral line-of-sight for path-following of underwater snake robots, in: Proc. IEEE Multi-Conference on Systems and Control, Juan Les Antibes, France. pp. 1078 – 1085.

Kohl, A.M., Kelasidi, E., Mohammadi, A., Maggiore, M., Pettersen, K.Y., 2016a. Planar maneuvering control of underwater snake robots using virtual holonomic constraints. Bioinspiration & Biomimetics 11.

Kohl, A.M., Kelasidi, E., Pettersen, K.Y., Gravdahl, J.T., 2015a. A control-oriented model of underwater snake robots exposed to currents, in: Proc. IEEE Conf. Control Applications, Sydney, Australia.

Kohl, A.M., Kelasidi, E., Pettersen, K.Y., Gravdahl, J.T., 2017. Model-based LOS path-following control of planar underwater snake robots, in: Fossen, T., Pettersen, K.Y., Nijmeijer, H. (Eds.), Sensing and Control for Autonomous Vehicles. Springer International Publishing. volume 474 of *Lecture Notes in Control and Information Sciences*.

Kohl, A.M., Pettersen, K.Y., Kelasidi, E., Gravdahl, J.T., 2015b. Analysis of underwater snake robot locomotion based on a control-oriented model, in: Proc. IEEE Int. Conf. Robotics and Biomimetics, Zhuhai, China. pp. 1930–1937.

Kohl, A.M., Pettersen, K.Y., Kelasidi, E., Gravdahl, J.T., 2016b. Planar path following of underwater snake robots in the presence of ocean currents. IEEE Robotics and Automation Letters 1, 383–390.

Liljebäck, P., Pettersen, K.Y., Stavdahl, Ø., Gravdahl, J.T., 2012. A review on modelling, implementation, and control of snake robots. Robotics and Autonomous Systems 60, 29–40.

Liljebäck, P., Pettersen, K.Y., Stavdahl, Ø., Gravdahl, J.T., 2013. Snake Robots: Modelling, Mechatronics, and Control. Springer-Verlag, Advances in Industrial Control.

Ma, S., 1999. Analysis of snake movement forms for realization of snake-like robots, in: Proc. IEEE International Conference Conference on Robotics and Automation (ICRA), Detroit, MI USA. pp. 3007–3013.

Ma, S., 2001. Analysis of creeping locomotion of a snake-like robot. Advanced Robotics 15, 205–224.

McIsaac, K., Ostrowski, J., 2003. Motion planning for anguilliform locomotion. IEEE Transactions on Robotics and Automation 19, 637–625.

Mohammadi, A., Rezapour, E., Maggiore, M., Pettersen, K.Y., 2014. Direction following control of planar snake robots using virtual holonomic constraints, in: Proc. IEEE 53rd Conf. Decision and Control, Los Angeles, CA, USA.

Mohammadi, A., Rezapour, E., Maggiore, M., Pettersen, K.Y., 2015. Maneuvering control of planar snake robots using virtual holonomic constraints. IEEE Trans. Control Syst. Technol. 24, 884 – 899.

Newman, J., 1977. Marine Hydrodynamics. MIT Press.

Nijmeijer, H., Schaft, A.v.d., 1990. Nonlinear Dynamical Control Systems. Springer-Verlag, New York.

Ostrowski, J., Burdick, J., 1996. Gait kinematics for a serpentine robot, in: Proc. IEEE Int. Conf. Robotics and Automation, pp. 1294–1299.

Panteley, E., Lefeber, E., Loria, A., Nijmeijer, H., 1998. Exponential tracking control of a mobile car using a cascaded approach, in: Proc. IFAC Workshop on Motion Control, pp. 221 – 226.

Panteley, E., Loria, A., 2001. Growth rate conditions for uniform asymptotic stability of cascaded time-varying systems. Automatica 37, 453 – 460.

Pettersen, K.Y., Egeland, O., 1996. Exponential stabilization of an underactuated surface vessel, in: Proc. 35th IEEE conf. Decision and Control, pp. 967–972.

Prautsch, P., Mita, T., Iwasaki, T., 2000. Analysis and control of a gait of snake robot. Trans. Institute of Electrical Engineers of Japan 120-D, 372–381.

Saito, M., Fukaya, M., Iwasaki, T., 2002. Serpentine locomotion with robotic snakes. IEEE Contr. Syst. Mag. 22, 64–81.

Sanders, J., Verhulst, F., Murdock, J., 2007. Averaging Methods in Nonlinear Dynamical Systems (Applied Mathematical Science). volume 59. Springer.

Sanfilippo, F., Azpiazu, J., Marafioti, G., Transeth, A.A., Stavdahl, Ø., Liljebäck, P., 2017. Perception-driven obstacle-aided locomotion for snake robots: The state of the art, challenges and possibilities. Applied Sciences 7.

Sans-Muntadas, A., Kelasidi, E., Pettersen, K.Y., Brekke, E., 2017. Spiral path planning for docking of underactuated vehicles with limited fov, in: Proc. 1st IEEE Conference on Control Technology and Applications, Kohala Coast, Hawaii.

Seibert, P., Florio, J., 1995. On the reduction to a subspace of stability properties of systems in metric spaces. Ann. Matematica Pura Appl. 169, 291–320.

Sfakiotakis, M., Lane, D., Davies, J., 1999. Review of fish swimming modes for aquatic locomotion. IEEE Journal of Oceanic Engineering 24, 237–252.

Skjetne, R., Fossen, T., Kokotović, P., 2004. Robust output maneuvering for a class of nonlinear systems. Automatica 40, 373–383.

Sverdrup-Thygeson, J., Kelasidi, E., Pettersen, K.Y., Gravdahl, J.T., 2016a. A control framework for biologically inspired underwater swimming manipulators equipped with thrusters, in: Proc.10th IFAC Conference on Control Applications in Marine Systems (CAMS), Trondheim, Norway.

Sverdrup-Thygeson, J., Kelasidi, E., Pettersen, K.Y., Gravdahl, J.T., 2016b. Modeling of underwater swimming manipulators, in: Proc.10th IFAC Conference on Control Applications in Marine Systems (CAMS), Trondheim, Norway.

Sverdrup-Thygeson, J., Kelasidi, E., Pettersen, K.Y., Gravdahl, J.T., 2017a. The underwater swimming manipulator – a bio-inspired solution for subsea operations. cond. accepted IEEE Journal of Oceanic Engineering .

Sverdrup-Thygeson, J., Moe, S., Pettersen, K.Y., Gravdahl, J., 2017b. Kinematic singularity avoidance for robot manipulators using set-based manipulability tasks, in:

Proc. 1st IEEE Conference on Control Technology and Applications, Kohala Coast, Hawaii.

Tanaka, M., Matsuno, F., 2014. Control of snake robots with switching constraints: trajectory tracking with moving obstacle. Advanced Robotics 28, 415–429.

Teel, A., Praly, L., 1995. Tools for semiglobal stabilization by partial state and output feedback. SIAM Journal on Control and Optimization 33, 1443–1488.

Tesch, M., Lipkin, K., Brown, I., Hatton, R., Peck, A., Rembisz, J., Choset, H., 2009. Parameterized and scripted gaits for modular snake robots. Advanced Robotics 23, 1131–1158.

Transeth, A.A., Pettersen, K.Y., Liljebäck, P., 2008. A survey on snake robot modeling and locomotion. Robotica 27, 999–1015.

Wang, J., Chen, S., Tan, X., 2013. Control-oriented averaging of tail-actuated robotic fish dynamics, in: Proc. of American Control Conference (ACC), Washington, DC. pp. 591–596.

Wiens, A., Nahon, M., 2012. Optimally efficient swimming in hyper-redundant mechanisms: control, design, and energy recovery. Bioinspiration & Biomimetics 7, 046016.

Wright, C., Johnson, A., Peck, A., McCord, Z., Naaktgeboren, A., Gianfortoni, P., Gonzalez-Rivero, M., Hatton, R., Choset, H., 2007. Design of a modular snake robot, in: Proc. IEEE/RSJ Int. Conf. Intelligent Robots and Systems, pp. 2609–2614.